HIGH-RESOLUTION CHEMOSTRATIGRAPHY OF THE WOODBINE AND EAGLE FORD GROUPS, BRAZOS BASIN, TEXAS

A Thesis

by

MELISSA JEAN MEYER

Submitted to the Office of Graduate and Professional Studies of
Texas A&M University
in partial fulfillment of the requirements for the degree of

MASTER OF SCIENCE

Chair of Committee,	Michael Pope
Committee Members,	Arthur Donovan
	Jerome Schubert
Head of Department,	Michael Pope

May 2018

Major Subject: Geology

ABSTRACT

Whole-rock elemental data is a useful tool for sub-dividing and characterizing mudrock variability across a shale basin. The chemostratigraphy of the Cenomanian-Turonian the Woodbine and Eagle Ford Groups in the Brazos basin—a western sub-basin of the East Texas basin—contains five distinct chemofacies within five regionally correlative chemozones, EB 1 through EB 5. Chemozones are characterized by variations in geochemical data and coincide with major sequence stratigraphic surfaces determined from gamma-ray and deep-resistivity wireline logs. Chemostratigraphic correlations of high-resolution XRF measurements (1.2 to 2.4-inch spacing; 12,282 total data points), integrated with 623 XRD mineralogy and 708 core-derived TOC measurements, highlight significant vertical and lateral elemental heterogeneities in a shale that otherwise appears to be homogenous.

In the Woodbine and Eagle Ford Groups, several key elements are identified and correlated to depositional conditions: Ca concentrations indicate carbonate input; Si, Al, K, and Ti concentrations indicate clay input; Mo and Mn concentrations indicate redox conditions; and Ni enrichment indicates paleoproductivity. These key elemental proxies characterize chemofacies and chemozones. Average concentrations of key elements were mapped across chemozones to quantify their regional variability across the basin. This chemostratigraphic framework highlights major changes in: sedimentation type (i.e. siliclastic versus carbonate), sea level, redox conditions, paleoproductivity, and organic-matter enrichment in source rock plays. This assessment ultimately aids identifying horizontal landing zones and understanding their spatial variation in source rock plays.

ACKNOWLEDGEMENTS

I would like to express gratitude to Apache Corporation for providing the cores, data, funding, and support for this project. I am extremely grateful for the mentorship and guidance of Ann Hudson, without which this work would not have been possible. Gratitude is extended to Frank Sheppard, Mark Olson, and Tad Smith for encouraging and supporting this endeavor. Thank you also to Martin Gibson and Travis Johnston for their mentorship and knowledge. Thank you to Brian Coffey for helping locate and access cores, operate the XRF spectrometers, and photograph thin section images. Thank you to Scott Brooks and Hawkwood Energy for granting access to a significant portion of the cores within this study. Thank you to Casey Donahue for collecting and synthesizing rebound hammer data. Thank you to Stephanie Sosol and Grace Craven for aiding the XRF data collection. Finally, thank you Aaron Carr and Cynthia Blaine for technological support.

CONTRIBUTORS AND FUNDING SOURCES

This work was supported by a thesis committee consisting of Professor Michael Pope and Professor Arthur Donovan of the Department of Geology, and Professor Jerome Schubert of the Department of Petroleum Engineering. Data, core access, and full funding was provided by Apache Corporation. Data and core access were also provided by Hawkwood Energy. Average TOC maps in Figure 12 were generated by Travis Johnston of Apache Corporation. All other work conducted for the dissertation was completed by the student independently.

TABLE OF CONTENTS

Page

LIST OF FIGURES

LIST OF TABLES

1. INTRODUCTION

In recent years, shale plays have risen to the forefront of hydrocarbon exploration in North America. A sharp growth in United States oil production—increasing from 5 MMBOPD in 2008 to 9.4 MMBOPD in 2016 (U.S. Energy Information Administration, 2016)—can in large part be attributed to the development of these unconventional resources. The Eagle Ford Group shale play of Maverick basin, Brazos basin, and the adjoining areas of Texas (Figure 1) has proven to be one of the most prolific unconventional resource plays worldwide. Although this trend was identified as productive as early as 1933 (McCallum, 1933), the economic conditions, drilling and completions technology, and geologic modeling needed to unlock commercial-level returns was not achieved until 2008 (Cusak et al., 2010).

Despite the undeniable success of unconventional resource plays, much has yet to be understood about the controls of organic matter (OM) richness and reservoir quality in shale formations. Understanding and modeling depositional environment is critical to identifying the most productive areas within a shale basin. Geochemistry and chemostratigraphy also are powerful forensic tools for determining variations in depositional conditions in shale units that otherwise appear homogenous (Brumsack, 2006; Tribovillard et al., 2006; Algeo and Rowe, 2012). The distribution, enrichment, and/or depletion of certain major and trace elements in fine-grained mudrock corresponds to particular sedimentary facies, implies specific paleoredox conditions, and results in OM richness consequences (Tribovillard et al., 2006; Algeo and Rowe, 2012). The chemostratigraphic interpretation of elemental variability allows for the quantitative spatial correlation of paleoenvironmental data across a basin. Basin-scale evaluations of depositional environment—when integrated with production, reservoir, and TOC data—aid in

determining source rock richness, optimal reservoir facies, hydrocarbon storage potential, ideal acreage positions, and horizontal well target zones of shale plays (Brumsack, 2006).

Exploitation of the organic-rich Eagle Ford Group as an oil, condensate, and gas shale play spans from the south Texas Maverick basin, across the San Marcos Arch, and into the Brazos sub-basin of the larger East Texas basin (Figure 1). Industry activity within the Eagle Ford Group has primarily occurred in the area southwest of the San Marcos Arch where extensive chronostratigraphic and geochemical studies were conducted (Wehner et al., 2017; Donovan et al., 2016; Donovan et al., 2015; Tinnin and Darmaoen, 2016; Moran, 2013; Kearns, 2011; Ratcliffe, 2011; Deluca, 2016). The Brazos basin chronostratigraphic equivalents to the prolific south Texas Eagle Ford Group have proven to be a sizable economic source of hydrocarbons. In this area, the Middle Cenomanian to Late Turonian sediments of the Eagle Ford and Woodbine Groups are stratigraphically, mineralogically, and geochemically distinct from the units in south Texas due to stronger influences from the (Early Cenomanian to Middle Cenomanian) Woodbine and (Turonian) Harris Delta systems (Adams and Carr, 2010; Donovan et al., 2015).

In this study, a chemostratigraphic framework is established for the Woodbine and Eagle Ford Groups from 10 cored wells, (A through J), throughout the Brazos basin (Figure 1; Table 1). A total of 12,282 x-ray fluorescence (XRF), 623 x-ray diffraction (XRD) mineralogy, and 708 core-derived total organic carbon (TOC) measurements were integrated in order to define five chemofacies that vary in mineralogy (argillaceous-to-calcareous) and OM content (poor-to-rich). Vertical changes in chemofacies and elemental signatures were used to sub-divide the strata into five chemostratigraphic zones which coincide with major chronostratigraphic surfaces (Donovan, 2017, unpublished). Key elements associated with OM enrichment were identified

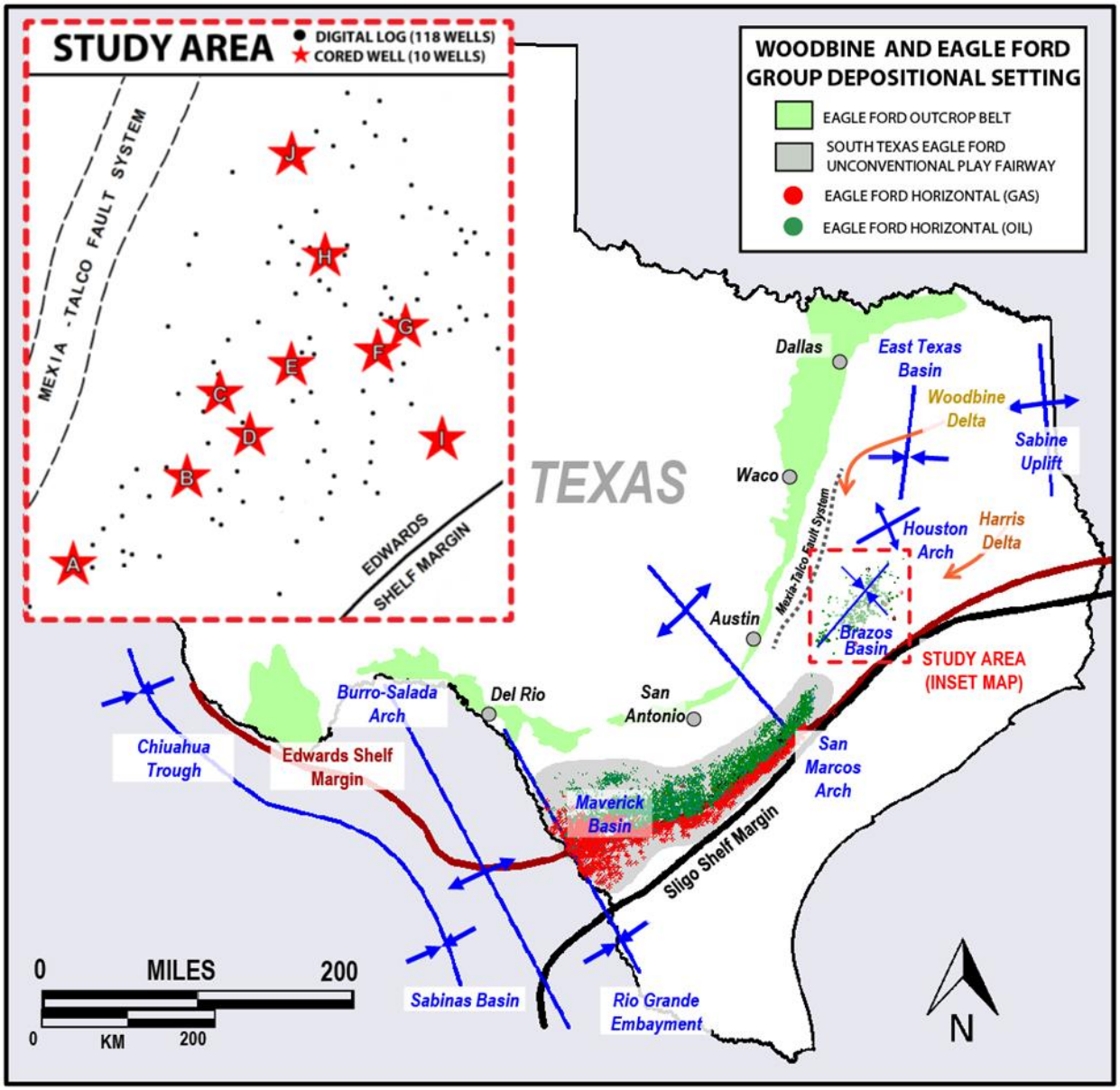

Figure 1. Map of Texas showing the Eagle Ford Group outcrop belt, productive Eagle Ford Shale trend, and major structural features during the Late Cretaceous. The Brazos Basin and focus area for this study is denoted with a red rectangle and shown in the inset map. Modified from Wehner et al., 2017 and Donovan et al., 2015. Oil and gas well spots taken from IHS production data (IHS, 2018).

and spatial changes in these elements were quantified by mapping average values in each chemozone across the basin. The chemozones were extrapolated to 118 wells throughout the

Table 1. Core data (XRF, XRD, TOC) for each of the ten wells, labelled A through J, in this study. For proprietary purposes, well names and locations have been omitted.

Study Label	Core Length (FT)	XRF Points	XRD Points	TOC Points
A	150'	1,499	60	117
B	266'	1,311	28	28
C	252'	1,262	133	23
D	268'	1,334	146	52
E	270'	1,350	20	121
F	209'	1,047	44	101
G	300'	1,491	84	178
H	250'	1,205	24	25
I	89'	437	84	63
J	272'	1,346	0	0
TOTAL	2,326'	12,282'	623	708

MD = Measured Depth; XRF = X-Ray Flourescence;
XRD = X-Ray Diffraction; TOC = Total Organic Carbon

basin by correlating gamma-ray and deep-resistivity wireline log characteristics. This chemostratigraphic framework quantifies major shifts in environment (e.g. OM productivity, redox conditions, and detrital input) during deposition and allows for a better assessment of the source- and reservoir-rock potential.

1.1 Geologic History

1.1.1 Structural Setting

The East Texas basin was one of several actively-subsiding extensional depocenters caused by early rifting along the Gulf Coast during the Mesozoic and Cenozoic (Mancini, 2008), forming concurrently with the Laramide Orogeny. The Brazos basin is considered to be a

western sub-basin of the East Texas basin (Figure 1), the axis of which trends parallel to the shelf margin (Denne and Breyer, 2016). The Brazos basin is separated from the East Texas basin by the northeast-southwest trending Houston Arch; stratigraphy and facies distribution on either side are distinctly different. Like the East Texas basin, the Brazos basin is structurally bounded to the west by the Mexia-Talco Fault System and by the Sabine Uplift to the northeast (Figure 1). Inactive Sligo and Stuart City reefs formed paleotopography along the shelf margin during deposition, providing restriction to the Brazos basin (Donovan et al., 2012). The Sabine Uplift and the erosion of the Ouachita and Arbuckle Mountains to the northeast provided much of the deltaic sediments within the older Woodbine (Woodbine Delta) and younger Eagle Ford (Harris Delta) Groups.

Across the entirety of Texas, the Woodbine/Eagle Ford succession is underlain by the Buda Formation and overlain by the Austin Chalk Formation (Figure 2). During deposition, the

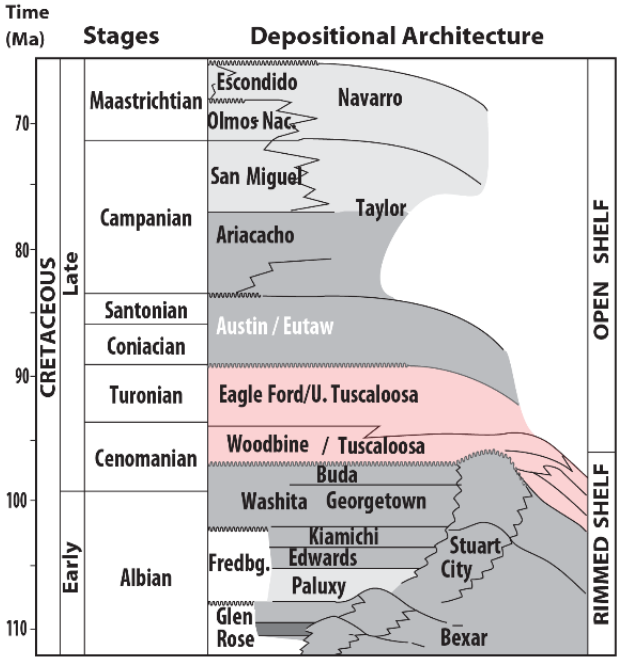

Figure 2. Generalized Cretaceous stratigraphic succession and architecture of the Northern Gulf of Mexico Basin with the Eagle Ford and Woodbine Groups highlighted in pink. Modified from Galloway, 2008.

San Marcos Arch effectively separated south and east Texas, causing significant controversy in the correlation of the Cenomanian/Turonian sediments across the arch (e.g. Vallabhaneni et al., 2016; Donovan et al., 2015; Hentz et al., 2014; Hentz and Ruppel, 2010). The Eagle Ford Group is a Middle Cenomanian to Late Turonian, unconformity-bounded, chronostratigraphic unit occurring in both south and east Texas (Donovan et al., 2015; Donovan, unpublished, 2017). The Woodbine Group is an older (Early to Middle Cenomanian), unconformity-bounded, siliclastic unit that underlies the Eagle Ford Group. It predominantly occurs in the east Texas basin as a productive sandstone of the Woodbine Delta (Figure 1), is present as a prodelta mudstone throughout the Brazos basin and rarely occurs southwest of the San Marcos Arch (Donovan et al., 2015).

1.1.2 Sequence Stratigraphic Framework

The complex depositional architecture of the Cenomanian-Turonian Gulf Coast sediments has resulted in multiple and conflicting naming systems for the Woodbine and Eagle Ford Groups. The chemozone boundaries (Figure 3) identified within this study are conformable with the nomenclature system and key chronostratigraphic surfaces of Donovan (2017).

Prior to Woodbine and Eagle Ford Group deposition, the Gulf Coast shelf was carbonate-dominated system (Phelps et al., 2010). The Buda Group consists of both the Buda Limestone Formation and the overlying False Buda Formation which is intermittently present in the Brazos and East Texas basins. In the study area, the False Buda Formation is thin but present and the unit's top marks the base of the study interval. A sea-level fall during the Early Cenomanian partially eroded the Buda Group. Subsequent eustatic sea-level rise formed the Western Interior Seaway (Arthur and Sageman, 2005) and deposited the Woodbine and Eagle Ford Groups throughout the Brazos basin.

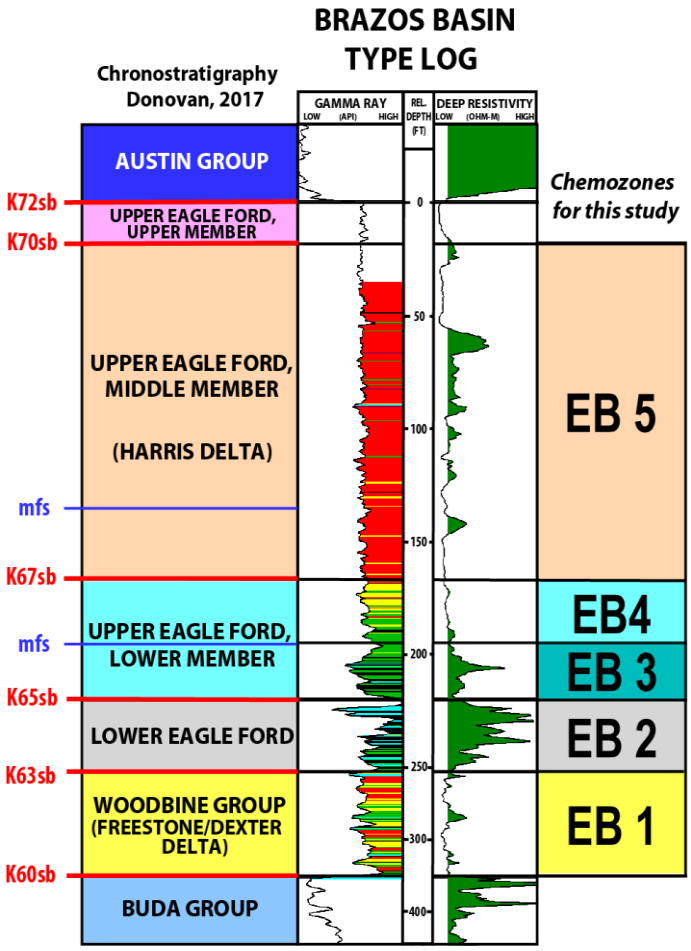

Figure 3. Type log (Core B) for the Eagle Ford and Woodbine Groups in the Brazos basin. Five chemozones are identified in this study and shown to the right of the type log. Chemozones are coincident with major chronostratigraphic surfaces identified by Donovan (2017), shown to the left of the type log.

The first sequence deposited above the Buda Group is the Woodbine Group (Figure 3) consisting of mudstone that prograded from the Woodbine Delta (Donovan et al., 2015). This regressive unit has characteristically low gamma-ray and deep-resistivity values and contains sediments that are systematically truncated from the top-down by the sequence boundary at the bottom of the overlying Lower Eagle Ford Member of the Eagle Ford Group (Donovan et al.,

2015; Adams and Carr, 2010). In the East Texas basin, the Woodbine Group exceeds 600 feet in thickness and contains productive sandstone beds. This unit thins to less than 100 feet in the Brazos basin and occurs predominantly as a pro-delta mudstone (Donovan, 2015). This unit commonly is confused with the younger Harris Delta sediments of the overlying Eagle Ford Group (e.g. Hentz and Ruppel, 2011) and may be also incorrectly interpreted in some literature as being age-equivalent to the Lower Eagle Ford (e.g. Denne and Breyer, 2016; Hentz and Ruppel, 2011).

The Lower Eagle Ford Formation is a distinctive sequence marked by high gamma-ray and deep-resistivity values. This unit is chronostratigraphically equivalent to the productive, organic-rich Lower Eagle Ford of south Texas. The Lower Eagle Ford Formation is a transgressive, calcareous, black shale and is the dominant target zone for horizontal drilling in the Brazos basin. Carbonate content of the Lower Eagle Ford Member is largely biogenic in origin and supplied by planktonic foraminifer shells (Hudson, 2014). The Lower Eagle Ford Formation and the Woodbine Group together are sometimes named the Maness Shale (e.g. Hentz and Ruppel, 2011; Denne and Breyer, 2016).

The overlying Upper Eagle Ford Formation is sub-divided into Upper, Middle, and Lower units (Figure 3). The Upper Eagle Ford Formation occurs across both south and east Texas, but is distinctly more clay-rich in the Brazos basin due to siliclastic input from the Harris Delta System than its calcareous equivalents in south Texas (Figure 3). The Lower Member of the Upper Eagle Ford Formation is transitional in lithology from an open-marine, carbonate-dominated lithology to a progressively more argillaceous, pro-delta mudstone of the Harris Delta. These deltaic sediments cause much of the thickening of the Eagle Ford Group within the Brazos basin. This unit has high-to-moderate gamma-ray and deep-resistivity log responses. The

Middle Member of the Upper Eagle Ford Formation is a regressive sequence of generally argillaceous and OM-poor mudstone that records distal deposits of the Harris Delta (Donovan et al., 2015). The Upper Member of the Upper Eagle Ford Formation is another regressive sequence sourced from the Navarro Delta to the east (Donovan, 2017). The sequence is thin to absent in the Brazos basin study area.

The Eagle Ford Group is overlain by an angular unconformity that formed prior to the Austin Chalk Formation, which was deposited as flat-lying beds in a deeper, quiet water shelf over both the basins and the uplifts of the Eagle Ford Group across Texas (Adams and Carr, 2010).

1.2 Controlling Factors on Source Rock Development

Organic-matter (OM) enrichment within source-rocks is governed by the interactions of three mechanisms: (1) preservation, (2) productivity, and (3) dilution (Bohacs et al., 2005). Understanding the relationships between these mechanisms, organic content, and the elemental composition of shales is key to reducing exploration risk in unconventional resource plays (Katz, 2012; Bohacs et al., 2005). A mudrock's enrichment and/or depletion in major elements (Ca, Si, Al, Fe, Mg, *etc.*) and trace elements (Mo, V, Cr, U, Ni, *etc.*) can be used as proxies for the primary mechanisms for OM-rich source-rock deposition (Sageman and Lyons, 2004; Jarvis, 1992; Tribovillard et al., 2006; Algeo and Rowe, 2012).

OM preservation is defined as the net accumulation and destruction of organic material within source rocks and is governed by the oxidation state of the water column at the time of deposition (Bohacs et al., 2005). An anoxic water column is devoid of aerobic biological activity; this condition occurs at the sediment-water interface where oxygen demands from

biologic productivity at the surface exceeds oxygen supplied by water circulation (Tribovillard et al., 2006). Many studies have concluded that anoxic depositional environments increase OM preservation and source rock potential (e.g. Demaison and Moore, 1980; Hollander et al. 1991).

OM productivity is the degree to which OM formation occured within the water column at the time of deposition. Productivity is largely associated with nutrient-enriched surface waters in oceanic upwelling zones that encourage microbial blooms (Harris, 2005). Certain organophyllic trace elements [such as copper (Cu), nickel (Ni), zinc (Zn), cadmium (Cd), and to a lesser extent phosphorous (P) and barium (Ba)] are preferentially enriched in organic molecules themselves (Tribovillard et al., 2006). Ni and Cu are especially excellent paleoproductivity proxies as they behave as micronutrients for plankton and typically indicate the preservation of deposited settling planktonic debris within anoxic mudrocks (Algeo and Rowe, 2012; Tribovillard et al., 2006; Hudson, 2014).

OM dilution is defined as the organic-carbon-free sedimentation rate (Tyson, 1995 from Bohacs et al., 2005). There is an optimal amount of dilution that maximizes OM accumulation and preservation; too much dilution will prohibit significant concentrations of OM accumulation, whereas too little dilution will limit preservation and burial, keeping OM at the surface and exposing it to microbial reworking, erosion, and transport (Tribovillard et al., 2006).

2. METHODS

2.1 High-Resolution XRF Acquisition

Energy dispersive x-ray fluorescence (ED-XRF) data were collected using two Bruker Tracer 5i handheld spectrometers (serial numbers 900F4196 and 900F4198) on all ten cores. Data were collected every 1.2" (3.0 cm) on Core A and every 2.4" (6.0 cm) on the remaining cores (Core B through Core J). Significant testing was conducted on Core F to establish the following collection parameters for this study: (1) data collected using both spectrometers was quantitatively comparable because data variance between the two machines is negligible for these cores; (2) a 15-second collection time for both trace and major elements was used because data variance between 15-, 30-, 90-, and 120-second collection intervals is negligible for these cores; (3) all cores were washed to eliminate potential surface impurities, however data variance between a washed and unwashed sample is negligible for these cores; (4) the metal guard plate originally installed on both handheld spectrometers was removed for all testing as it significantly increases the distance between the scintillometer and the sample, decreasing the concentration of all readings.

Both scintillometers were calibrated using the mudrock reference matrices developed by Rowe et al. (2012). All data were collected within ten days during May and June of 2017. On each core, the 900F4198 spectrometer was used to scan from the top-down and the 900F4196 spectrometer was used to scan from the bottom-up. The machines overlapped in data collection for fifty measurements in the middle of the each core to confirm that the production of quantitatively comparable results. Before and after scanning, a metal token with a specific

elemental composition was measured to assure that there was no instrument drift. Before a core was scanned, the entire section was washed thoroughly with warm tap water and wiped in the direction of bedding planes. The handheld devices were positioned face-down on the slabbed core face for scanning. Care was take to position the gun flush with the surface of the slab, avoiding fractures or irregular surfaces. Trace and major elements were collected sequentially within a single scan using the dual mode of the handheld devices. In dual mode, the devices began scanning trace elements under a 15-kV filter for a 15-second count time. At 15 seconds, the filter automatically flips to a 40-kV filter and major elements are scanned for another 15 seconds.

Raw data for each scan recorded counts of photons versus energy signatures in kV. The raw-energy spectra for each individual scan is then converted to elemental concentrations using a proprietary method developed by Bruker. Data were output in spreadsheet format for each scan, denoting the elapsed time and elemental concentrations in weight percent. Concentrations in weight percent for 27 elements (Mg, Al, Si, P, S, K, Ca, Ti, V, Cr, Mn, Fe, Co, Ni, Cu, Zn, As, Rb, Sr, Y, Zr, Nb, Mo, Ba, Pb, Th, and U) were recorded. Three elements were poorly detected by the handheld: Cu, Ba, and U; these data were therefore omitted from the study. Significantly high concentrations of Ca (>25%) interfere with the detection of many trace elements (e.g. Ni, V, Mo, Cr, Zn). Therefore, any data showing this interference was removed when portraying cross-plot relationships of these trace elements with other data. Ashbeds and phosphatic nodules commonly plotted as outliers so these also were omitted and generally avoided, if possible, during data collection. At any point where a plug was visibly extracted for XRD mineralogy or TOC data analysis, care was taken to collect an XRF measurement as close as possible to the

plug hole. Where available, data were compared to benchtop XRF data collected by Core Lab on crushed samples to check measurement accuracy.

2.2 Spotfire Cluster Analysis of Chemofacies

Elemental chemofacies were derived by running an agglomerative hierarchical cluster analysis of the combined XRF data on all wells within the study using TIBCO Spotfire software. This is a statistical grouping method that clusters individual data points into a tiered dendrogram of similar groups. Spotfire's cluster analysis is powerful because it not only clusters similar rows of data (i.e. rows of elemental data for associated depths), but also clusters similar columns of data (i.e. detrital elements which track each other, e.g. Si, K, Al, and Ti, will cluster together). A variety of clustering methods are available in TIBCO Spotfire; Ward's method was demonstrated to produce the best results in a variety of geologic studies (Roush, 2015; Temple et al., 2008) and was the method used within this study. Agglomerative hierarchical clustering using Ward's Method produces cluster combinations that minimize internal grouping variance (Romesburg, 1989). The cluster analysis normalizes the range of values for each column (i.e. Ca) between 0 and 1. This effectively normalizes the entire dataset such that major elements in wt % and trace elements in ppm are weighted equally and not based on concentration value.

A spreadsheet was created that contained all 12,282 rows of XRF data. Each row contained a core label (i.e. Core A through J) and a depth label. Each row contained column values for all 27 elements. The elemental data were then clustered by row, producing a dendrogram tree to visualize cluster relationships. Clustering of rows and columns using Spotfire is powerful because it groups depths that contain similar geochemical signatures across many cores. This allows us to quantitatively correlate rock sections with elementally similar

Table 2. Input parameters used to convert XRF elements to mineral compositions in Interactive Petrophysics. Mineral densities and clay ratios are calibrated to XRD data from the cores.

Mineral Densities (g/cm^3)		Chlorite Elemental Ratios	
Illite	**2.70**	*Aluminum, Al*	**8.12**
Kspar	**2.57**	*Silica, Si*	**12.69**
Anhydrite	**2.98**	*Iron, Fe*	**20.80**
Pyrite	**5.01**	*Magnesium, Mg*	**5.49**
Smectite	**2.35**		
Plagioclase	**2.62**	**Smectite Elemental Ratios**	
Dolomite	**2.85**	*Aluminum, Al*	**9.83**
Calcite	**2.71**	*Silica, Si*	**20.46**
Siderite	**3.96**	*Magnesium, Mg*	**9.90**
Quartz	**2.65**		
Kaolinite	**2.60**	**Illite Elemental Ratios**	
Chlorite	**2.88**	*Potassium, K*	**4.50**
Apatite	**3.15**	*Aluminum, Al*	**11.50**
TOC	**1.25**	*Silica, Si*	**24.90**
Fluid Density	**1.00**	*Iron, Fe*	**4.80**
Bulk Density	**2.60**	*Magnesium, Mg*	**2.05**
Clay Mineral Ratios		**Kaolinite Elemental Ratios**	
Clay : Feldspar	**0.75**	*Aluminum, Al*	**20.9**
Smectite : Kaolinite	**0.50**	*Silica, Si*	**21.76**
Chlorite : Siderite	**0.50**		

compositions (chemofacies) across multiple cores in a basin. Chemofacies groupings can be assigned on as low-level (only a few groups) or as high-level (many groups) as desired.

The data relationships function of Spotfire was used to determine which XRF elements were most linearly correlated (both positively and negatively) to TOC data. This helped to reduce the number of variables inputted into the final iteration of the hierarchical cluster analysis down to 5 key elements: Ca (positive correlation with TOC), Si (negative correlation with TOC), Mo (positive correlation with TOC, anoxia indicator), Mn (negative correlation with TOC, oxia indicator), and Ni (positive correlation with TOC, productivity indicator). In this way, the data

were able to be appropriately clustered into 5 meaningful chemofacies for this broad regional study.

When available, XRD mineralogy and TOC measurements produced by Core Labs were incorporated into the dataset. Rebound hammer data was also collected on a 1' (30.5 cm) resolution on Cores A, E, F, and G using a Proceq Bambino Rebound Hammer. The device gives readings in Leeb Hardness, which is defined as the ratio of rebound velocity to impact velocity of a rebounding ball within the hammer. Uniaxial compressive strength (UCS) is then calculated from Leeb Hardness measurements by the following equation for clay-rich mudstone (Lee et al., 2014):

$$\text{UCS (MPa)} = 2.154e^{0.0058x} \text{ where } x = \text{Leeb Hardness}$$

2.3 Element-to-Mineral Conversion of XRF Data

A proprietary element-to-mineral conversion program, developed by Michael Ashby of Apache Corporation, within Interactive Petrophysics was used to approximate the mineralogical composition of core samples from XRF elemental data. This conversion tool uses weight percent concentrations for Ca, Al, Si, Fe, Mg, S, K, Th, and P to derive mineral concentrations at each measurement. Parameters for the application are summarized in Table 2. Element-to-mineral conversions were particularly useful in order to fraction terrigenous quartz and feldspars from clay.

2.4 Enrichment Factor Calculation

Particular trace elements were normalized by calculating enrichment factors (EF), which compare sample data of a certain element to concentrations from a known reference source. The

reference source chosen for this study was the Post Archean Average Shale (PAAS) from Taylor and McClennan (1985). Element enrichment factors are calculated by the following equation:

$$\mathrm{EF}_{\mathrm{Element}} = \frac{\dfrac{\mathrm{Element\ Concentration\ (ppm)}_{\mathrm{Sample}}}{\mathrm{Aluminum\ Concentration\ (ppm)}_{\mathrm{Sample}}}}{\dfrac{\mathrm{Element\ Concentration\ (ppm)}_{\mathrm{PAAS}}}{\mathrm{Aluminum\ Concentration\ (ppm)}_{\mathrm{PAAS}}}}$$

If EF is greater than 1, the element is enriched and if EF is less than 1, the element is depleted. This method was used in particular for calculating enrichment factors in the trace elements Mo and Ni.

3. RESULTS

3.1 General Geochemical Trends and Elemental Proxies

Complete profiles of geochemical data, gamma-ray and resistivity log responses, TOC data, and XRD mineralogy are contained in Appendix A. Several definitive trends in the elemental and rock data occur within the Woodbine and Eagle Ford Groups. Cross-plots of calcium (Ca) and total carbonate minerals (calcite, dolomite, and siderite) from XRD data shows a moderate positive, linear relationship (Figure 4A). Of the total carbonate minerals detected in XRD data, 77% are calcite, 9% are dolomite, and 14% are siderite. Cross-plotting Ca and TOC shows a positive correlation until Ca concentration exceed approximately 25 wt%, after which an inversely correlative trend is observed (Figure 5A).

Terrigenous elements are clearly defined when cross-plotting them with Titanium, which is typically overwhelmingly terrigenous in origin (Tribovillard et al., 2006). By these methods, the following major elements (Figure 4E) are determined to be strongly detrital: silica (Si), aluminum (Al), potassium (K), and titanium (Ti). Trace-elements including Pb, Nb, Rb, Y, and Th also show linear relationships with Ti and are interpreted to be detrital in origin. Strongly-linear Si/Ti (Figure 4E) correlations suggest that there is rarely a biogenic Si fraction within the dataset. Strongly-linear Si/Al (Figure 4D) correlations suggest that the majority of the Si resides within the clay fraction and not within sand or silt fraction (Ratcliffe et al., 2007).

Cross-plotting the sum of the major terrigenous elements (Si + Al + K + Ti) with the total clay minerals from XRD data (Figure 4B) shows a moderate positive correlation, confirming that these element are detritally-sourced and reside largely within the clay fraction. This composite

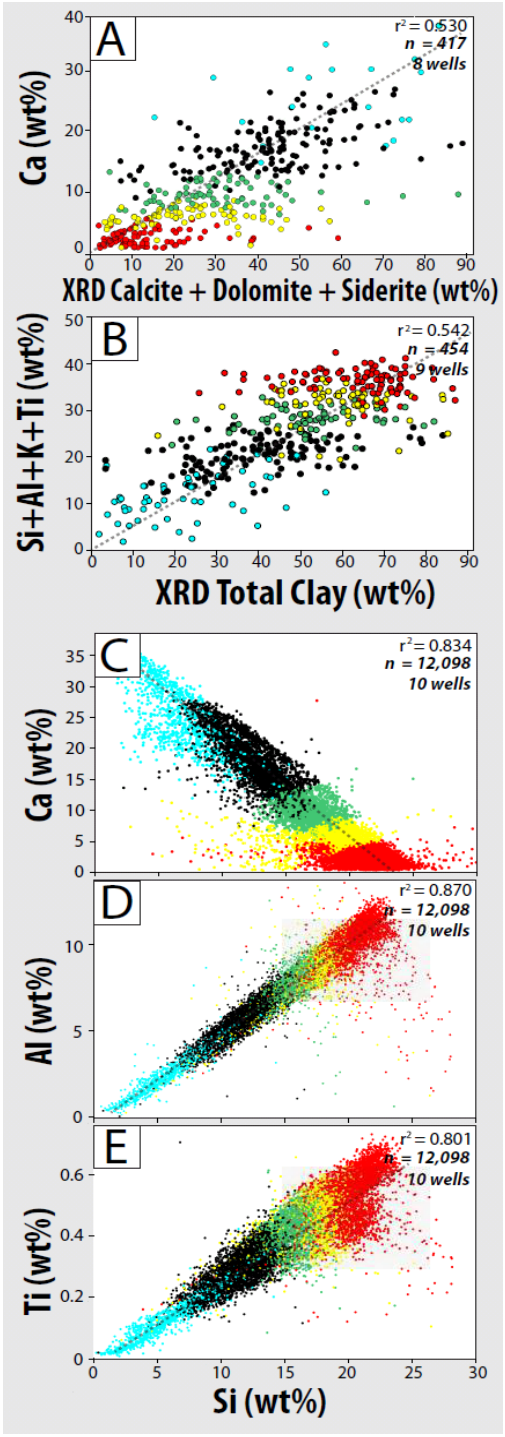

Figure 4. Cross-plots of elemental data with XRD minerals (A and B) and silica (C, D, and E). Data is colored by chemofacies, a legend for which is shown in Figure 6.

Table 3. Summary of the defining characteristics of each chemofacies.

Chemofacies Statistics		Argillaceous, OM-Poor	Transitional, OM-Poor	Transitional, OM-Moderate	Calcareous, OM-Rich	Calcareous, OM-Moderate
Dominant Lithology Observed in Thin Section		Laminated silty-claystone	Laminated claystone	Argillaceous, foraminiferal marlstone	Laminated foraminerferal marlstone	Dolomitized foraminiferal wackestone
Measurement Statistics	Total Number of Measurements	4,061	1,964	2,118	3,030	550
	Percentage of Total Measurements	33%	16%	17%	24%	5%
	Total Represented Footage of Core	812'	393'	423'	606'	110'
Elemental Averages	*Carbonate Content:* Ca (wt%)	2%	6%	9%	17%	25%
	Terrigenous Content: Si + Al + K + Ti (wt%)	37%	32%	29%	21%	10%
	Oxygen Indicator: Mn (ppm)	325	241	175	116	262
	Anoxia Indicator: EF Mo	10	16	20	33	47.1
	Paleoproductivity Indicator: EF Ni	0.45	0.71	0.73	1.20	2.27
XRD Mineralogy Averages	Total Measurements in Chemofacies	173	99	96	181	42
	Total Carbonate (wt%)	24%	26%	30%	40%	50%
	Total Clay (wt%)	46%	47%	44%	36%	27%
	Quartz and Feldspar (wt%)	17%	15%	12%	15%	15%
TOC	Total TOC Measurements in Chemofacies	160	78	72	161	32
	Average TOC (wt%)	1.47%	2.42%	2.81%	3.70%	2.85%
Rebound Hammer Strength	Total Number of Measurements in Chemofacies	514	194	185	360	58
	Average Uniaxial Compressive Strength	2915 psi	3088 psi	3443 psi	4512 psi	6368 psi
Log Properties	Average Resistivity (Ohm-m)	3.22	3.31	4.00	8.78	9.65
	Average Gamma-Ray (API)	103	102	105	108	102

curve of major terrigenous elements can be considered as a proxy for terrigenous input. Ca/Si (Figure 4C) correlations demonstrate a strong inverse relationship. This reciprocal relationship also is clearly demonstrated by plotting elemental data converted to oxides on a ternary diagram (Figure 6) with end-members of 5x Al_2O_3—2x CaO—SiO_2 (Brumsack, 1989).

Three significant trends between trace elements and TOC are shown in Figure 5. Mo (Figure 5C) demonstrates a weakly positive correlations to TOC. Mn (Figure 5E) demonstrates a moderate, inverse correlation to TOC. EF Ni (Figure 5D) demonstrates a moderate positive correlation with TOC.

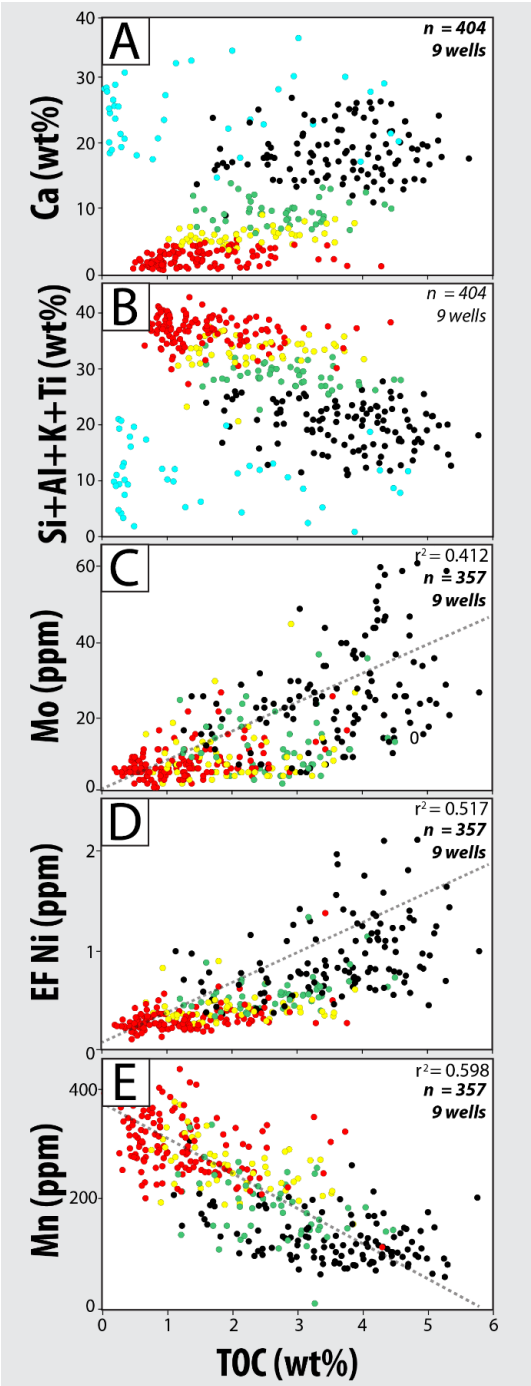

Figure 5. Cross-plots of elemental data with TOC data. Data is colored by chemofacies, a legend for which is shown in Figure 6.

3.2 Chemofacies Definitions

Clustering of key elements (i.e. Ca, Si, Mo, Mn, and Ni) produced five distinct chemical facies, summarized in Table 3: (1) argillaceous, OM-poor; (2) transitional, OM-poor; (3) transitional, OM-moderate; (4) calcareous OM-rich; and (5) calcareous, OM-moderate.

3.2.1 Argillaceous, OM-Poor

The argillaceous, OM-poor chemofacies (Figures 6, 7, and 8A) are defined by the highest values of terrigenous elements (Si, Al, K, and Ti) and Mn and the lowest values of Ca, Mo, and Ni measured within this study (Table 3). This is the most common chemofacies, representing 33% of the total dataset. XRD mineralogy confirms that this chemofacies is the lowest in carbonate and highest in terrigenous clay, quartz, and feldspar. Average TOC content in this chemofacies is the lowest of all chemofacies. Uniaxial compressive strength (UCS) indicates that this is the mechanically weakest chemofacies, averaging 2915 psi. Spectral gamma-ray and deep-resistivity average values are relatively low.

In thin section, this chemofacies is observed as a silty-claystone (Figure 8A) with laminations consist dominantly of light brown, terrigenous clay, moderate amounts of silt, and occasional globigerinid foraminifera. Foraminifera commonly are clay or pyrite- filled. Disseminated pyrite occurs occasionally within the laminations. In hand sample this chemofacies is dark brown and fissile, breaking easily along bedding planes.

3.2.2 Transitional, OM-Poor

The transitional, OM-poor chemofacies (Figure 6, 7, and 8B) are defined by significantly elevated concentrations of terrigenous elements and Mn and significantly reduced concentrations of Ca, Mo, and Ni (Table 3). This chemofacies records a slight decrease in terrigenous input and

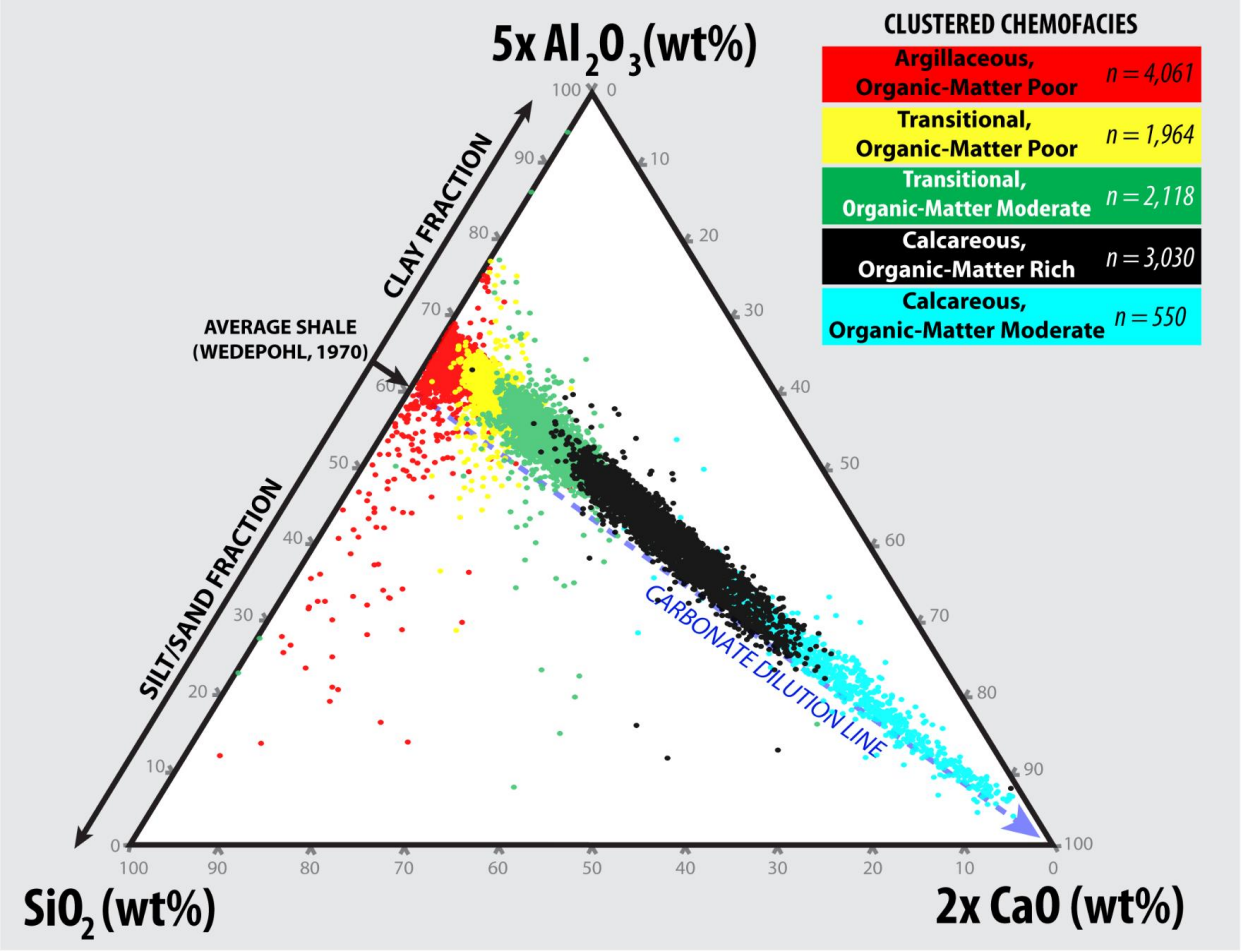

Figure 6. Ca-Si-Al oxide ternary diagram (modeled after Brumsack, 1989), colored by chemofacies. The Woodbine and Eagle Ford Groups are largely a binary system between clay and carbonate. n= total number of measurements.

slight increase in carbonate content as compared to the argillaceous, OM-poor chemofacies. This chemofacies comprises 16% of the total measurements and represents a transitional facies that is dominantly argillaceous but has a small carbonate component. The XRD mineralogy confirms low carbonate content and high terrigenous clay, quartz and feldspar content. Average TOC content is low but not as low as the argillaceous, OM-poor chemofacies. UCS values indicate that this unit is relatively weak, averaging 3088 psi. Spectral gamma-ray values and deep-resistivity values remain low.

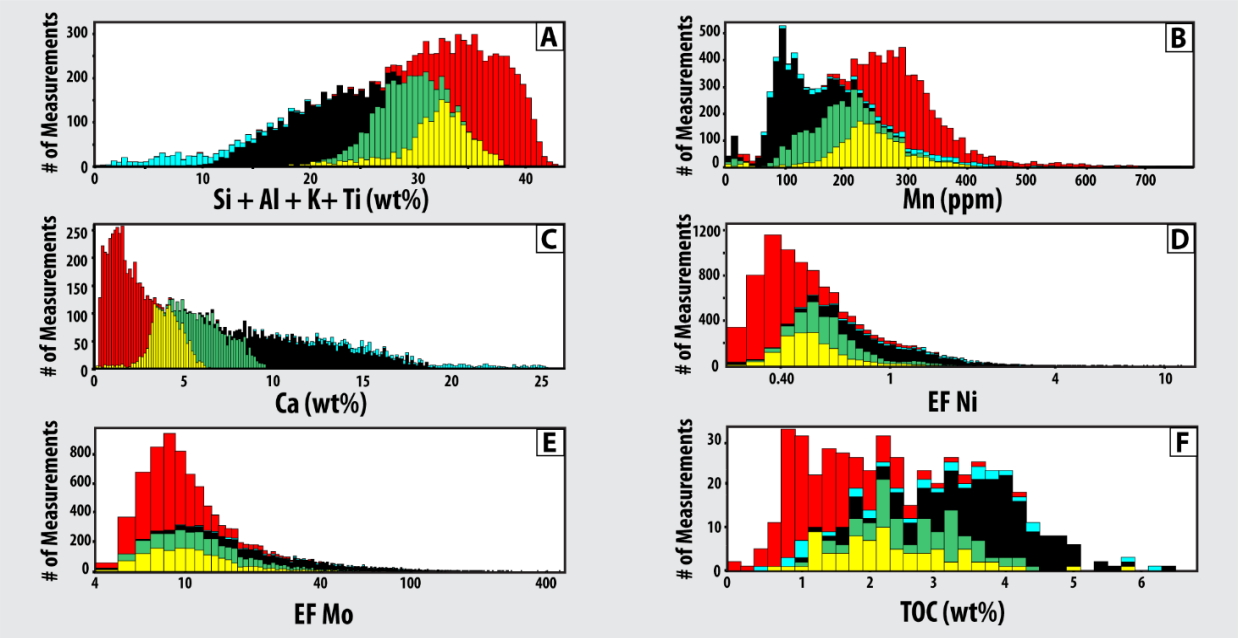

Figure 7. Histogram distributions of key elements and TOC, colored by chemofacies compositions. A color legend for chemofacies is shown in Figure 6.

foraminiferal laminations (Figure 8B). Less silt-sized quartz and feldspar grains and more clay laminations are seen in its thin sections compared to the argillaceous, OM-poor facies. Light brown terrigenous clay is still visually dominant in thin section, but black, calcareous mud is increasingly more common. In hand sample, this chemofacies is dark brown to black with visible bedding planes, but is generally less-fissle than the argillaceous, OM-poor facies.

3.2.3 Transitional, OM-Moderate

The transitional, OM-moderate chemofacies (Figures 6, 7, and 8C) are defined by moderate concentrations of all key elements and represents 17% of the total dataset (Table 3). This transitional facies is significantly more enriched in Ca and depleted in terrigenous elements than the transitional, OM-poor chemofacies. The XRD mineralogy confirms the increase in carbonate content and decrease in siliclastic content within the elemental chemistry. Average

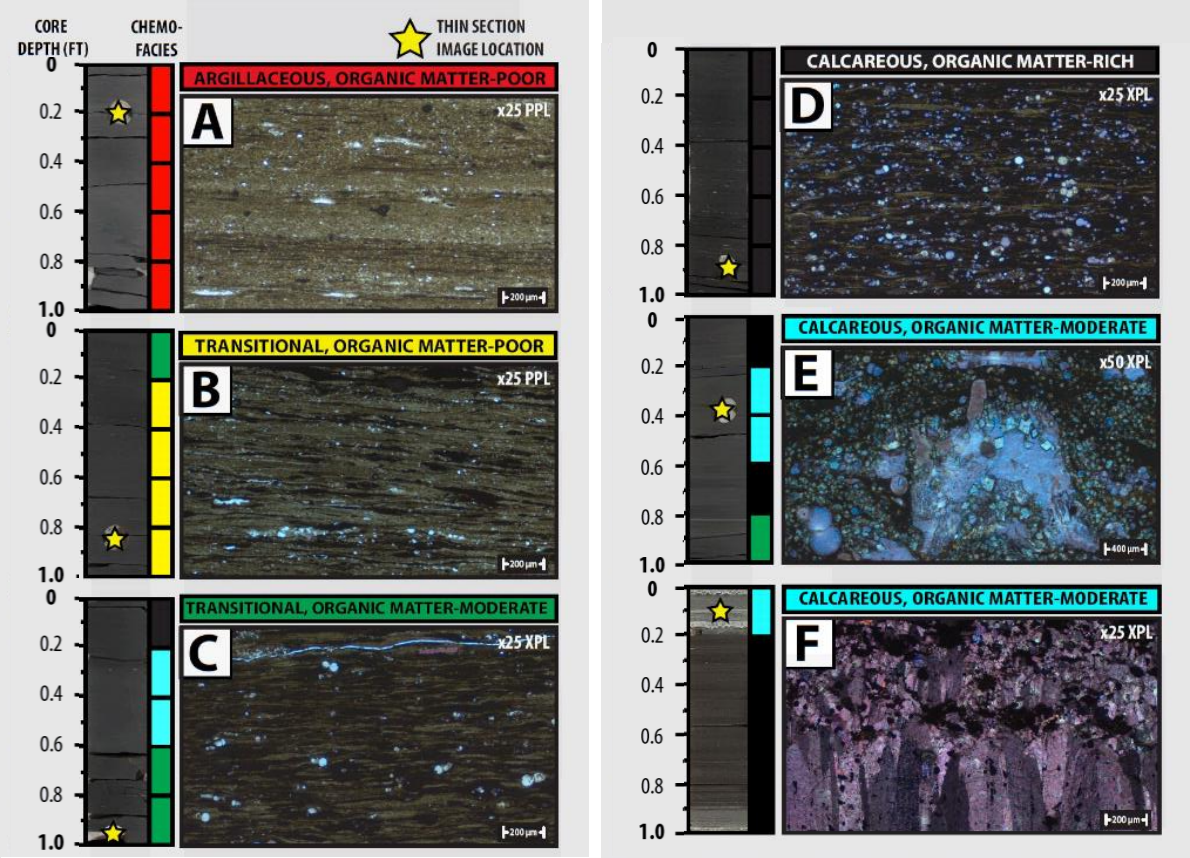

Figure 8. Representative photomicrographs of the dominant lithologies observed in each chemofacies. **(A)** laminated silty-claystone observed in the argillaceous, OM-poor chemofacies; **(B)** laminated claystone observed in the transitional, OM-poor chemofacies; **(C)** argillaceous, foraminiferal marlstone observed in the transitional, OM-moderate chemofacies; **(D)** laminated, foraminiferal marlstone observed in the transitional, OM-rich chemofacies; **(E)** dolomitized foraminiferal wackestone observed in the calcareous, OM-moderate chemofacies; and **(F)** fibrous calcite cement observed in the calcareous, OM-moderate chemofacies. Core photograph and thin section image location is shown to the left of each photomicrograph. Thin-section images A-D and F were taken from Core E of this study; thin-section image E was taken from Core D.

TOC content is moderate in this chemofacies. UCS values indicate that this chemofacies is moderate in relative mechanical strength, averaging 3443 psi. Spectral gamma-ray values are slightly elevated and deep-resistivity readings are moderate.

The transitional, OM-moderate chemofacies represents an argillaceous, foraminiferal marlstone (Figure 8C; Allix et al., 2010). In thin section, black calcareous mud is dominant with secondary amounts of light-brown, terrigenous clays. Calcite-filled globigerinid foraminifera are very common and weakly-to-moderately laminated. Inoceramid shells are occasionally present. In hand sample, this chemofacies is rarely fissile and dominantly black, however lighter grey laminations occur where carbonate-rich foraminifers are concentrated.

3.2.4 Calcareous, OM-Rich

The calcareous, OM-rich chemofacies (Figure 6, 7, and 8D) is the most organic-rich facies within the Woodbine and Eagle Ford succession and is defined by the highest enrichment in Mo and Ni, high concentrations of Ca, low concentrations of terrigenous elements, and the lowest concentrations of Mn within the total dataset (Table 3). It represents 24% of the total measurements. XRD mineralogy confirms high concentrations of total carbonate minerals and relatively low terrigenous minerals (quartz, feldspar, and clay). Average TOC content in the calcareous, OM-rich chemofacies is the highest the highest of all chemofacies. Rebound hammer measurements indicate high mechanical strength compared to more argillaceous facies, averaging a UCS of 4512 psi. Spectral gamma-ray and deep-resistivity values are the highest in the entire data set.

The calcareous, OM-rich chemofacies dominantly is a laminated, foraminiferal marlstone (Figure 8D). Planktonic foraminifera and black calcareous mud dominate thin sections. Light-brown, terrigenous clay occurs minimally compared to the more argillaceous chemofacies.

Inoceramid shells are common and aligned with bedding planes. Foraminifera shells are usually calcite-filled and/or rimmed by calcite. In hand sample, this chemofacies is dominantly black with common, lighter laminations containing higher concentrations of foraminifera.

3.2.5 Calcareous, OM-Moderate

The calcareous, OM-moderate chemofacies (Figure 6, 7, 8E, and 8F) occurs as the most calcareous facies and is defined by the highest concentrations of Ca, moderate concentrations of Mn, low concentrations of Mo and Ni, and the lowest concentrations of terrigenous elements of all chemofacies (Table 3). The calcareous, OM-moderate chemofacies represents only 5% of the entire dataset. XRD mineralogy supports the elemental data, indicating the lowest amount of clay and highest amount of carbonate minerals occur in this chemofacies. Average TOC content is approximately equivalent to the transitional, OM-moderate chemofacies. This chemofacies demonstrates the highest mechanical strength, averaging a UCS of 6368 psi, and it has high deep-resistivity values, and low spectral gamma gamma-ray values.

The calcareous, OM-moderate chemofacies represents two distinct lithofacies when analyzed in thin section (Figures 8E and 8F), both enriched in diagenetic carbonate. The most dominant lithofacies is a dolomitized, foraminiferal wackestone (Figure 8E). In this facies, ferroan dolomite partially-to-fully replaces abundant globigerinid foraminifera and commonly rims disaggregated inoceramid shells. Fine, euhedral ankerite crystals commonly occur within the black, calcareous mud matrix of this lithofacies. The secondary lithofacies observed within this chemofacies cluster is a thinly-bedded fibrous, calcite cement (Figure 8F) that fill bedding-parallel factures. Calcite fibers in these veins grow normal to bedding and are colloquially called “beef-texture calcites” for their resemblance to fibrous steak (Al Duhailan et al., 2015; Cobbold and Rodrigues, 2007). In hand sample, beef-texture calcites occur as massive, grey-colored

Table 4. Summary of the defining elemental characteristics of each chemozone and resulting interpretations for paleoenvironment.

Chemo-zone	Defining Elemental Trends	Dominant Chemofacies	Paleoenvironment Interpretation			
			Dominant Sediment Source	Redox Conditions	Organic Matter Productivity	Source Rock Quality
EB 5	**High:** Al, Si, K, Ti, Mn **Low:** Ca, Mo, Ni, V	Argillaceous, OM-Poor	Terrigenous Clay	Highly Oxic	Low	Poor
EB 4	**High:** Al, Si, K, Ti, Mn **Low:** Ca, Mo, Ni, V	Transitional, OM-Poor	Terrigenous Clay	Oxic	Low	Poor
EB 3	**Increasing Upward:** Al, Si, K, Ti, Mn **Decreasing Upward:** Ca, Mo, Ni, V	Transitional, OM-Moderate	Upward transition from Carbonate to Clay	Suboxic	Moderate	Fair to Good
EB 2	**High:** Ca, Mo, Ni, V **Low:** Si, Al, K, Ti, Mn	Calcareous, OM-Rich	Pelagic Carbonate	Anoxic	High	Excellent
EB 1	**High:** Al, Si, K , Ti **Moderate:** Ca, Mo, Mn, Ni, V	Argillaceous, OM-Poor	Terrigenous Clay, Localized Pelagic Carbonate	Suboxic	Moderate	Fair to Poor

laminations ranging in thickness from 5 mm to 10 cm. The calcareous, OM-moderate chemofacies appears light grey in color due to higher concentrations of carbonate minerals. Vertical fractures ranging from 10 to 30 cm commonly observed in core, corresponding with an increase in mechanical strength, brittleness and calcite content. Almost always, this chemofacies is interbedded within thick packages of the calcareous, OM-rich chemofacies.

3.3 Chemozone Definitions and Elemental Maps

The Woodbine and Eagle Ford Groups were sub-divided into five regionally correlative chemozones, EB 1 through EB 5, by identifying shifts in elemental data and chemofacies occurrence that coincide with major chronostratigraphic surfaces (Figure 9). The defining elemental trends for each chemozone and resulting paleoenvironmental interpretation are summarized in Table 4. North-south and west-east regional correlations of chemozones between cored wells are shown in Figure 10. For complete geochemical profiles for each core in this study, see Appendix A. Structure maps produced for each chemozone depict a uniform,

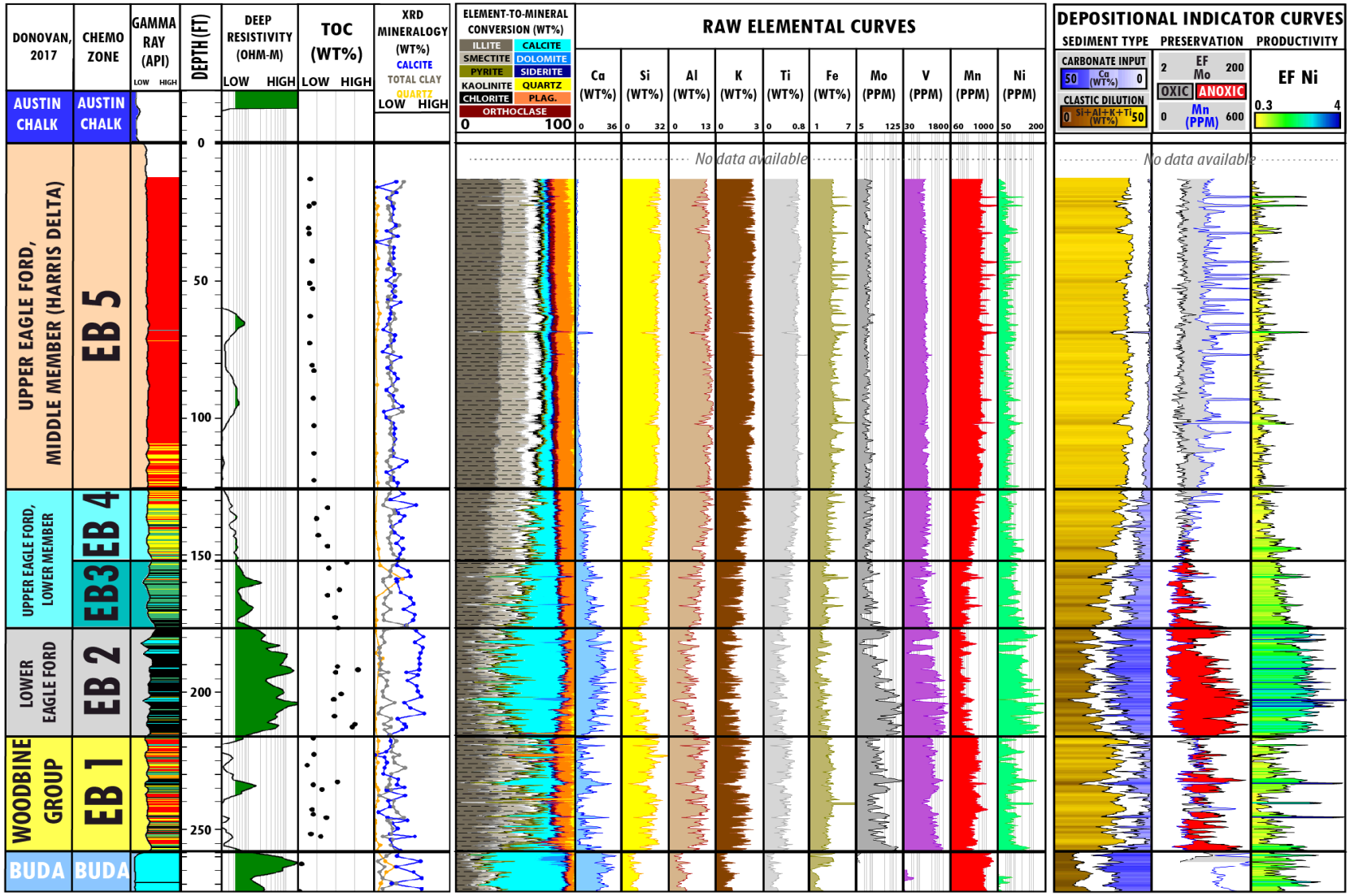

Figure 9. Geochemical profiles for Core D as correlated to TOC, XRD mineralogy, gamma-ray logs and deep-resistivity logs. Depositional indicator curves are key elemental curves that indicate variations in organic matter dilution, preservation, and productivity. Well location is shown in Figure 1. Chemofacies color legend is shown in Figure 5. Element-to-Mineral conversions were conducted using the parameters outlined in Table 2. EF = enrichment factor.

monoclinal dip towards the southeast. Gross isopach maps (Figure 11) convey changes in thickness for each chemozone. Average values of elemental data in each chemozone across all wells were used to construct regional elemental maps for average Ca, quartz and feldspar (QF), total clay (TC), EF Ni, Mo, and Mn (Figures 13).

3.3.1 Chemozone EB 1

Chemozone EB 1 (Figure 9) corresponds to the entire Woodbine Group (Figure 2; Donovan, 2017) within the Brazos basin, which is bounded by unconformities and is deposited directly above the False Buda Formation of the Buda Group (Figure 10). Gamma-ray and deep-resistivity signatures for this chemozone are relatively low. EB 1 is weakly organic-rich, with an average TOC of 1.93 wt% across 103 measurements. The unconformity at the base of EB 1 is recognizable by a distinct shift from carbonate-dominated deposition in the False Buda Formation of the Buda Group (Ca > 30 wt%) to terrigenous-dominated deposition in EB 1. Terrigenous elements generally are high and argillaceous and transitional, OM-poor chemofacies are FALSE BUDA most dominant in EB 1, especially in the northern cores. Chemozone EB 1 thickening to the northwest (Figure 11) coincides with increased terrigenous input, as both the QF and TC maps for EB 1 illustrate increasing concentrations that coincide with EB 1 northwest thickening, where average calcium and Ni decreases, but Mn increases. Mo is most elevated in cores B, C, D, and E, forming a bullseye pattern of increasing concentration across the basin (Figure 11).

3.3.2 Chemozone EB 2

Chemozone EB 2 corresponds to the transgressive Lower Eagle Ford Formation (Figure 3; Donovan, 2017), which is the most organic-rich chemozone—averaging a TOC of 3.93 wt% across 95 measurements—and the target for most horizontal wells in the Brazos basin. Gamma-

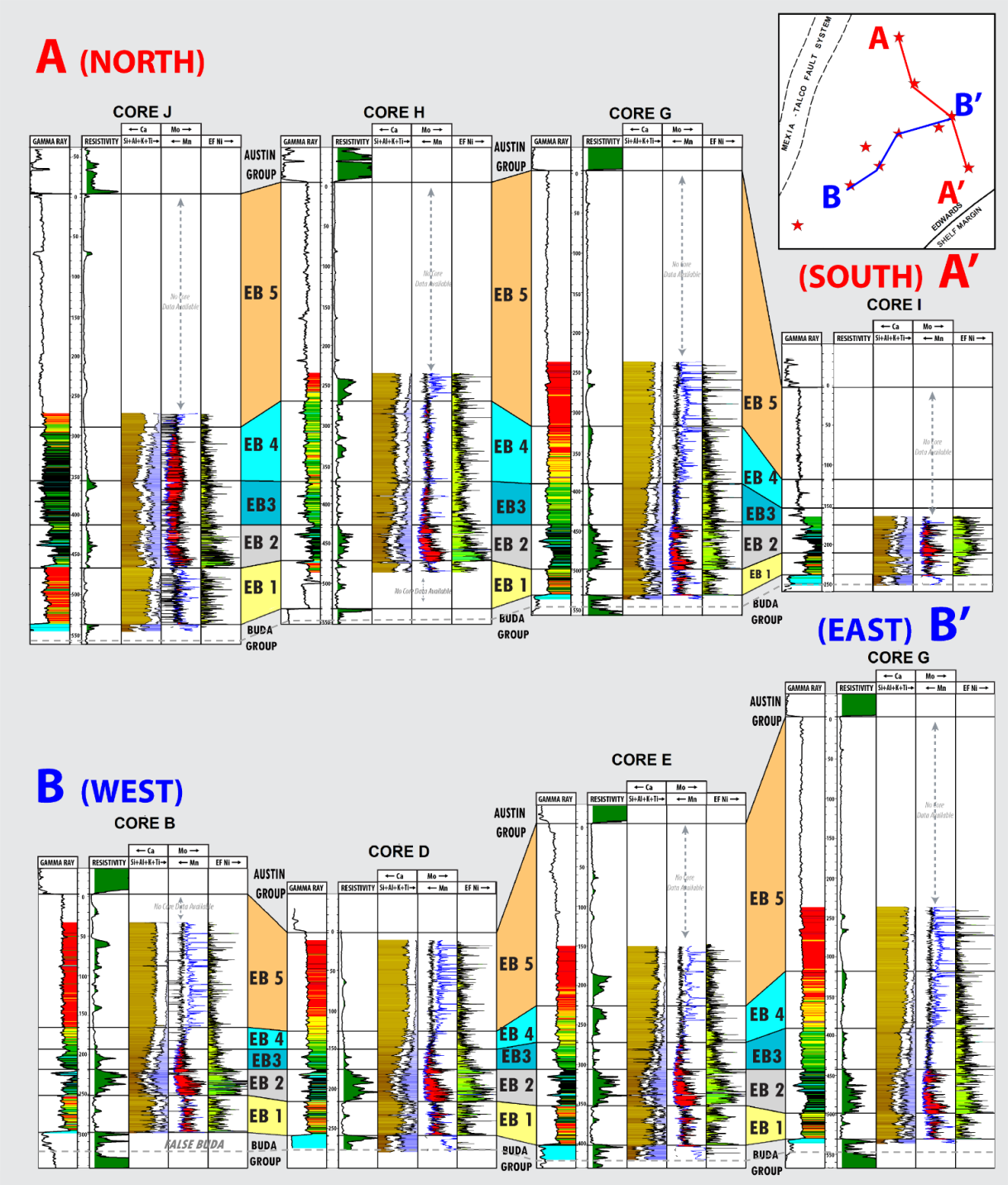

Figure 10. Regional cross sections A-A' (North-South) and B-B' (West-East) showing correlation of chemozones across the Brazos basin. Flattened on the top of chemozone EB2, which is interpreted to be the top of the Lower Eagle Ford Formation.

ray and deep-resistivity signatures are the highest in EB 2 of the entire succession (Figure 9). The unconformity at the base of EB 2 is recognizable by a distinct increase in Ca concentrations and decrease in terrigenous elements (i.e. Si, Al, K, Ti). EB 2 is defined by maximum concentrations of Ca, Mo, and EF Ni and minimum concentrations of QF, TC, and Mn of any chemozone. The calcareous, OM-rich chemofacies is the most dominant facies in EB 2 with secondary amounts of the calcareous, OM-moderate chemofacies. Mo concentrations are maximal and most enriched in cores B, C, and D in the center of the basin. Mn concentrations are minimal and most depleted in cores B, D, E, and J in the center of the basin. Ni is most enriched in this chemozone and shows increasing average concentrations in cores to the north and west. Chemozone EB 2 thickness increases to the northeast, coinciding with increases in QF and TC and decreases in Ca. Nonetheless, EB 2 is still the most carbonate-rich and siliclastic-poor chemozone within this study, as documented in the chemical maps and as seen in the element-to-mineral models for each core.

3.3.3 Chemozone EB 3

Chemozone EB 3 corresponds to the lower portion of the Lower Member of the Upper Eagle Ford Formation (Figure 3; Donovan, 2017). Gamma-ray and deep-resistivity values for this chemozone are moderate (Figure 9). EB 3 is moderately organic-rich, averaging a TOC of 3.06 wt%. In the center of the basin, this chemozone is characterized by a continual, upward decrease in Ca concentrations and increase in terrigenous element concentrations from minimal levels in EB 2. Elemental indicators also document a gradual upward decrease in Mo and EF Ni and an increase in Mn. The dominant chemofacies in EB 2 is transitional, OM-moderate with secondary amounts of the calcareous, OM-rich chemofacies. However, towards the north and west, a major facies change occurs and the calcareous, OM-rich facies is more dominant. This

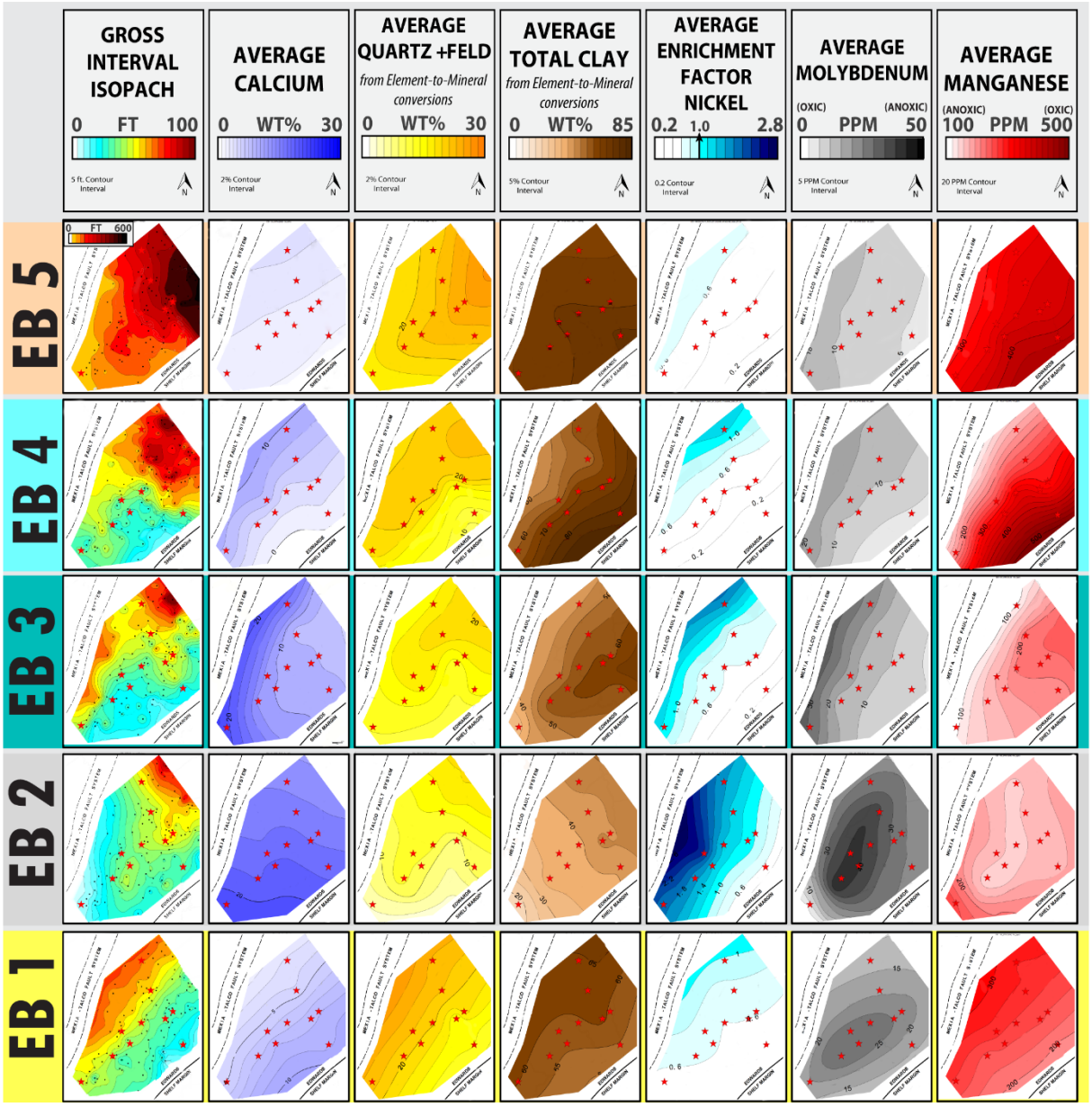

Figure 11. Gross interval isopachs and average elemental maps by chemozone. Gross interval isopachs are constructed by correlating chemozonations using gamma-ray and deep-resistivity logs from 118 wells across the basin. Elemental maps are constructed by contouring the average value per chemozone in each well across the basin. Quartz and feldspar (QF) and total clay (TC) maps are constructed from average mineral concentrations from Element-to-Mineral conversions. For each elemental map set, maps are color-scaled exactly the same such that relative changes across chemozones can be conceptualized.

trend is particularly evident in cores A and J (Figure 10). Chemozone EB 3 increases in thickness to the north and northwest (Figure 11) coinciding with increases in both carbonate concentration to the northwest and terrigenous element concentration to the northeast. Dramatic increases in average Ca concentration to the northwest coincides with the previously mentioned north and west facies transition to dominantly calcareous, OM-rich facies. Where this facies transition is observed (Cores A and J), EB 3 also shows enrichment of Mo and EF Ni and depletion Mn (Figure 11).

3.3.4 Chemozone EB 4

Chemozone EB 4 corresponds to the upper portion of the Lower Member of the Upper Eagle Ford Formation (Figure 3; Donovan, 2017). Gamma-ray and deep-resistivity values for this chemozone are relatively low. EB 4 is organic-poor, averaging 1.61 wt% TOC. EB 4 is defined at the base by a distinct increase in Mn and decrease in Mo concentrations (Figure 9). The transitional, OM-poor chemofacies is the most dominant chemofacies in EB 4. Terrigenous elements and Mn continue to increase-upward through EB 4 whereas Ca concentrations continue to decrease-upward. Mo and EF Ni are both depleted throughout the entire interval. Chemozone EB 4 thickness increases to the northeast, coincident with increases in QF to the east (Figure 11). Mn increases to the southeast, sub-parallel to increases in TC. Average Ca, Mo, and EF Ni maps all increase weakly to the northwest but their concentrations are generally very low.

3.3.5 Chemozone EB 5

Chemozone EB 5 corresponds to the Middle Member of the Upper Eagle Ford Formation (Figure 3; Donovan, 2017). Gamma-ray and deep-resistivity corresponding to this chemozone are the lowest for the entire succession. EB 5 is very organic-poor, averaging 0.94 wt% TOC. Chemozone EB 5 is defined at the base by a transition to fully-terrigenous sediment input

(Figure 9) indicated by the highest concentrations of terrigenous elements, the lowest concentrations of Ca, and the pervasiveness of argillaceous, OM-poor chemofacies throughout the entire chemozone. Mo and EF Ni consistently are very depleted and Mn concentrations consistently are very enriched throughout EB 5. Element-to-mineral conversions indicate increasing-upward concentrations of quartz. Chemozone EB 5 thickens dramatically to the northwest (Figure 11) coinciding with increased QF concentrations. Mn increases to the southeast, sub-parallel to increases in TC (Figure 11). Average concentrations of Ca, Mo, and EF Ni in EB 5 are the lowest of the entire data set and vary only weakly, increasing slightly to the northwest.

EB 5 is absent in Core A and only partially cored in wells E, G, H, and J. Operators commonly chose not to core the interval because it is exceedingly clay-rich and organic-matter poor. The elemental maps for EB 5 are therefore more interpretive.

4. DISCUSSION

4.1 Key Elements and their Implications for OM Enrichment

4.1.1 Ca as a Proxy for Carbonate Input

Ca concentration demonstrates a significant linear relationship with carbonate minerals (Figure 4A) from XRD (calcite, dolomite, and siderite) and is interpreted to represent the carbonate fraction of the total dataset. Increased carbonate content is generally favorable for organic matter enrichment (Figure 5A), however different types of carbonate have different implications for organic matter enrichment, a topic which is discussed in a following section.

4.1.2 Si + Al + Ti + K as a Proxy for Clay Input

The composite curve of Si + Al + Ti + K concentrations is interpreted to represent the terrigenous fraction of the dataset. Strong Si/Ti (Figure 4E) and Si/Al (Figure 4D) relationships indicate that there is a negligible biogenic silica fraction within the dataset and that a majority of the Si resides within the clay fraction. Therefore, Si + Al + K + Ti largely represent a terrigenous clay fraction, which is supported visually by thin section (Figure 8) and also in the significant linear trend between these elements and total clay minerals from XRD (Figure 4B). In the Woodbine and Eagle Ford Groups, organic matter dilution occurs primarily through terrigenous clay input; increases in terrigenous elemental concentrations often coincide with areas of large gross interval thickening and represent times of increased siliclastic sedimentation rates. Increasing concentrations of terrigenous elements clearly show a negative correlation with TOC (Figure 5B).

4.1.3 Mo as a Proxy for Anoxic Conditions

Organic matter preservation in source rocks is achieved largely through deposition within anoxic settings or stratified water columns (Katz, 2012; Bohacs et al. 2005) and Mo-enrichment is a classic indication for anoxia (Tribovillard et al., 2006; Brumsack, 2006; Calvert and Pedersen, 1993; Algeo and Rowe, 2012). Mo is a highly mobile element under oxidizing conditions but will fall out of solution under oxygen-poor conditions (Tribovillard et al., 2006). A positive Mo/TOC (Figure 5C) correlation in the Woodbine and Eagle Ford Groups indicates Mo-enrichment that is interpreted to occur under anoxic depositional conditions.

4.1.4 Mn as a Proxy for Oxic Conditions

Mn-enrichment is common during oxic bottom-water conditions (Calvert and Pedersen, 1993; Sageman and Lyons, 2003; Tribovillard et al., 2012; Brumsack, 2006). The moderate negative Mn/TOC (Figure 5E) correlation in the Woodbine and Eagle Ford Groups, and coincident Mn-enrichment is interpreted to indicate oxic depositional conditions.

4.1.5 Mo/Mn Crossover as a Proxy for Dominant Redox Condition

Mo and Mn indicate reciprocal conditions of water column oxygenation with Mo-enrichment indicating oxygen-poor depositional environments and Mn-enrichment indicating oxygen-rich depositional environments. Mo/Mn curve crossover (Figure 9) can therefore be used to highlight shifts in dominant redox conditions at the time of deposition (e.g. when Mn is to the left of Mo, conditions are oxic and when Mo when is to the left of Mn, conditions are anoxic).

4.1.6 EF Ni as a Proxy for OM Productivity

Ni is soluble in oxygenated, marine water columns and behaves as a micronutrient for microbial scavengers (Tribovillard et al, 2006). In stratified water columns or in areas of upwelling, scavengers will ingest Ni in the oxygenated surface waters and upon death will be

deposited and preserved at the anoxic sediment-water interface (Tribovillard et al., 2006). In the Woodbine and Eagle Ford Groups, moderate positive EF Ni/TOC (Figure 5D) correlations support the interpretation that EF Ni is a proxy for OM productivity.

4.2 Types of Carbonate and their Implications for Depositional Environment and OM Enrichment

Carbonate concentrations in the Woodbine and Eagle Ford Groups in the Brazos basin record pelagic carbonate deposition and subsequent diagenesis of that carbonate. Pelagic carbonate is composed of planktonic foraminifera and marine mudstone (Figure 8D), both of which are dominant in the calcareous, OM-rich chemofacies. The lack of biodiversity, low amounts of terrigenous dilution, depletion in Mn, and enrichment in Mo and Ni in this chemozone suggest a dominantly stressed, anoxic, and low-energy environment of deposition with high OM productivity. This type of pelagic carbonate demonstrates a positive correlation with TOC (Figure 5A, Figure 7F).

Two diagenetic alterations of these foraminifera-rich mudrocks occur the OM-moderate chemofacies: a dolomitized foraminiferal wackestone (Figure 8E) and a precipitated, fibrous calcite (Figure 8F). The dolomitized foraminiferal wackestone is the most common diagenetic calcareous facies in the dataset. In clay-rich mudstone, this type of ferroan dolomite can form in early diagenesis as magnesium releases during smectite-illite conversion (Zeng and Tice, 2014). The bed-parallel, fibrous calcite veins are hypothesized to precipitate during early diagenesis under exceedingly sulfidic, anoxic conditions in which methanogenic bacteria precipitate calcite (Zeng and Tice, 2014; Kruse, 2014). Both diagenetic carbonate features are replacive of the original rock fabric, diluting TOC. Ca/TOC (Figure 5A) correlations from the representative

calcareous, OM-moderate chemofacies are the only data that reflect decreasing TOC with increasing Ca concentration. Furthermore, this chemofacies is exceedingly high in mechanical strength and may be potential frac-barriers (Al Duhailan et al., 2015).

4.3 Reciprocal Sedimentation of Siliclastic and Carbonate Rocks

The biomodal nature of siliclastic and carbonate deposition in the Woodbine and Eagle Ford Groups is demonstrated clearly by the strong inverse nature of Ca and Si concentrations within the elemental dataset (Figure 5A). Average Ca maps (Figure 11) are largely inverse of average QF and TC maps. Siliclastic mudstones are interpreted to indicate a more proximal depositional environment, being deposited during sea level falls. Carbonate input is largely pelagic foraminifera and carbonate mud, which are interpreted to indicate a more distal shelf environment, being deposited during sea level rise.

Two distinct terrigenous systems are identified within the data set, which correspond to the Woodbine (EB 1) and Harris Delta systems (EB 3 through 5). The Woodbine prodelta mudstone deposits occurring EB 1 are defined by increasing average QF and TC concentrations to the northwest (Figure 11) and are interpreted to be deposited during an overall sea-level fall. A distinct shift from a northwesterly-sourced to northeasterly-sourced terrigenous input based on average elemental concentrations (Figure 11)—which coincides with gross interval thickening—between EB 1 to EB 2 suggests a major unconformity and/or stratigraphic change at this boundary. This boundary coincides with the sequence boundary that separates the Woodbine and Eagle Ford Groups within the Brazos basin (Donovan et al. 2015). EB 2 is characterized by maximum carbonate concentrations and minimum terrigenous input, indicating a more distal marine depositional environment and an overall higher sea level. The second terrigenous system

occurs in chemozones EB 3 through EB 5 and is associated with input from the Harris Delta from the northeast (Donovan et al., 2015). The system becomes increasingly more enriched in terrigenous elements upward through time, with maximal QF concentrations in EB 5, which is consistent with the interpretation that these chemozones are dominated by an overall sea level fall.

4.4 Paleoenvironment and Source Rock Quality by Chemofacies

The following depositional conditions are interpreted for each chemofacies (EB 1 through 5) based on their elemental definitions (Table 3) and their key elemental indicators.

4.4.1 Argillaceous, OM-Poor

Low Mo and high Mn indicate this chemofacies was deposited in an oxic water column. High concentration of terrigenous elements indicate that terrigenous dilution of OM is high. Low EF Ni values indicate low levels of paleoproductivity. This chemofacies is the most ductile and the most organic-poor, making it the poorest quality source rock and the least fracable chemofacies.

4.4.2 Transitional, OM-Poor

Low Mo and moderate Mn concentrations indicate this chemofacies was deposited in a suboxic water column. High concentrations of terrigenous elements indicate that terrigenous dilution of OM is high. Low EF Ni values indicate low levels of paleoproductivity. This chemofacies is ductile and organic-poor, making it a poor quality source rock that is undesirable for horizontal fracturing.

4.4.3 Transitional, OM-Moderate

Moderate Mo and low Mn concentrations indicate this chemofacies was deposited in an anoxic to suboxic water column. Moderate concentrations of terrigenous elements indicate that OM dilution is moderate. Moderate EF Ni values indicate moderate levels of paleoproductivity. This chemofacies has moderate mechanical strength and is moderately organic-rich, making it a moderate quality source rock for horizontal fracturing.

4.4.4 Calcareous, OM-Rich

High Mo and low Mn concentrations indicate this chemofacies was deposited in an anoxic to euxinic water column. Low concentrations of terrigenous elements indicate that OM dilution is low. High EF Ni values indicate high levels of paleoproductivity. This chemofacies is mechanically brittle and organic-rich, making it the best quality source rock for horizontal fracturing within the dataset.

4.4.5 Calcareous, OM-Moderate

Very high Mo concentrations and the occurrence of diagenetic carbonate indicates this chemofacies was deposited in a euxinic water column. High EF Ni values indicate very high levels of paleoproductivity. Low concentrations of terrigenous elements indicate low clay dilution, however in this chemofacies diagenetic carbonate dilutes TOC. This carbonate dilution is relatively small as this chemofacies represents only 5% of the total dataset. The “beef texture” calcites of this chemofacies are exceedingly high in mechanical strength and precipitated as bed-parallel planes, making them potential frac-barrier in horizontal wells (Al Duhailan et al., 2015).

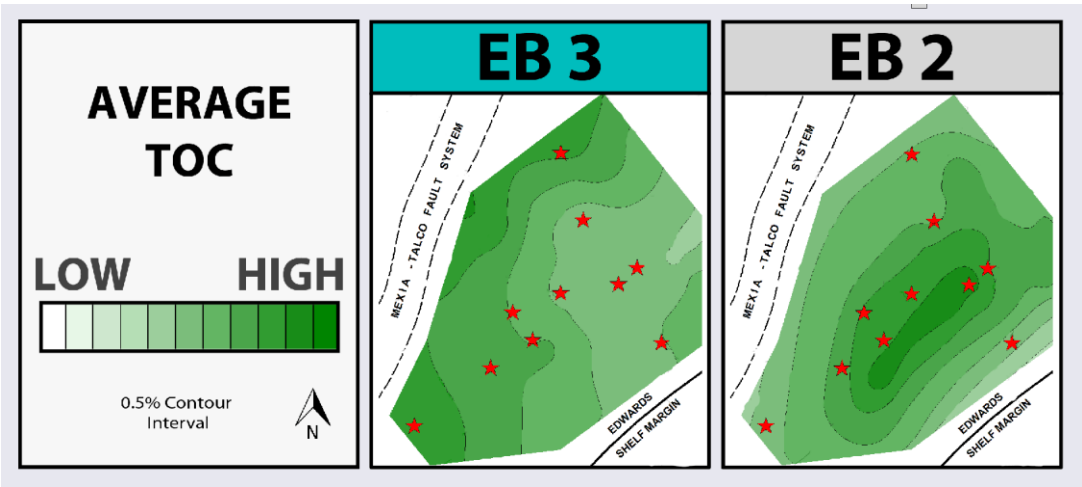

Figure 12. Average maps for the most organic-rich chemozones, EB 2 and EB 3. Average TOC co-varies with average Mo maps (Figure 11), suggesting that organic matter enrichment in the Brazos basin is largely driven by anoxia.

4.5 Paleoenvironment and Source Rock Quality by Chemozone

The following depositional conditions are interpreted for each chemozone based on their defining elemental trends (Table 4) and indications from key elemental indicators.

4.5.1 EB 1

High QF and TC concentrations indicate that OM dilution in EB 1 is high and increases toward the northwest. EF Ni concentrations indicate low levels of OM productivity. Mo concentrations indicate suboxic to anoxic conditions which are most enriched in the center of the basin (cores B, C, D, and E). Chemozone EB 1 contains poor-quality source rock and would make a poor landing zone for horizontal wells.

4.5.2 EB 2

Low QF and TC concentrations indicate that OM dilution in EB 1 is minimal, increasing slightly toward the northwest. EF Ni concentrations in this chemozone indicate the highest levels

of OM productivity throughout the basin. Average Mo and Mn concentrations indicate anoxic to euxinic conditions, which are most enriched in the center of the basin (cores B, wells. Covariance of average Mo and average TOC maps (Figure 12) suggest that reducing conditions are the most prominent driver in organic-matter enrichment within the Brazos basin.

4.5.3 EB 3

Chemozone EB 3 is enriched in Ca concentrations to the north and west (Cores A and J), indicating low OM dilution (Figure 11). Increases in EF Ni and Mo coincide with increases in Ca. Conversely, chemozone EB 3 is enriched in terrigenous elements to the south and east, indicating high OM dilution. Decreases in EF Ni and Mo coincide with increases in average QF and TC. Chemozone EB 3 contains good-quality source rock to the west and north, and poor-quality source rock to the south and east. This interpretation is supported by a map of average TOC in EB 3 (Figure 12).

4.5.4 EB 4

High average QF and TC concentrations indicate that OM dilution in EB 4 is high and increases toward the east. EF Ni concentrations indicate low levels of OM productivity. Mo concentrations indicate oxic conditions which increase slightly to the northwest. Chemozone EB 4 contains poor-quality source rock and would make a poor landing zone for horizontal wells.

4.5.5 EB 5

High average QF and TC concentrations indicate that OM dilution is high in EB 5 and increases toward the northeast (QF concentrations) and to the southeast (TC concentrations). EF Ni concentrations indicate very low levels of OM productivity and Mo concentrations indicate highly oxic conditions. Chemozone EB 5 contains poor-quality source rock and would make a poor landing zone for horizontal wells.

5. CONCLUSIONS

Even in the simplest of shale formations, mudstone deposition is complex and depends on a variety of depositional processes. Often, variability is only discernible on the micro-scale and requires a higher-resolution analysis. XRF data is inexpensive, simple to collect across many cores, and can be correlated to TOC and XRD mineralogy. Elemental proxies for mineralogy and organic-matter richness allow the interpretation chemostratigraphic boundaries and changes in regional depositional processes occurring within a shale basin. In the Woodbine and Eagle Ford Groups, several key elements are identified and correlated to depositional conditions: (1) Ca indicates carbonate input, which is associated with foraminifer deposition and generally favorable conditions for OM enrichment; (2) Si indicates terrigenous clay dilution and is unfavorable for OM enrichment; (3) Mo and Mn are inverse indicators of redox conditions at the time of deposition—high Mo and low Mn concentrations are generally favorable for OM preservation and enrichment; and (4) Ni records fluctuations in paleoproductivity and is favorable for OM deposition and enrichment.

Five statistically-clustered chemofacies are identified throughout the Woodbine and Eagle Ford Groups from elemental analysis and its relationships to TOC data: (1) argillaceous, OM-poor; (2) transitional, OM-poor; (3) transitional, OM-moderate; (4) calcareous, OM-rich; and (5) calcareous, OM-moderate. These chemofacies highlight the high-frequency variability within a visually homogeneous shale and have direct relationships with OM-richness.

Five chemozones, EB 1 through EB 5, are defined by variations in dominantly occurring chemofacies and major elemental shifts in which coincide with the proposed sequence stratigraphic framework (Donovan, 2017). Chemozone EB 1 corresponds to the Woodbine Group, is dominated by siliclastic input from the northwest, and was deposited in suboxic

conditions during a sea level fall with moderate OM productivity resulting in fair-to-poor source rock quality. Chemozone EB 2 corresponds to the Lower Eagle Ford Formation, contains minimal amounts of terrigenous clay dilution and high amounts carbonate input, was deposited under anoxic conditions during a sea level rise with high OM productivity resulting in the best source rock quality of all chemozones. Chemozone EB 3 corresponds to the lower portion of the Lower Member of the Upper Eagle Ford Formation, is high in carbonate content, was deposited under anoxic to suboxic conditions during a sea level fall with moderate OM productivity resulting in fair to good source rock quality. EB 4 and EB 5 are both dominated by siliclastic deposition from the east/northeast and were deposited under oxic to highly oxic conditions during prolonged sea level fall with low organic matter productivity resulting in poor source rock quality.

Regional chemostratigraphy highlights major changes in: sedimentation type (i.e. siliclastic versus carbonate), sea level, redox conditions, paleoproductivity, and organic-matter enrichment in source shale basins. This assessment ultimately aids identifying horizontal landing zones and understanding their spatial variation in source rock plays.

REFERENCES

Adams, R. L. and J. P. Carr, 2010, Regional depositional systems of the Woodbine, Eagle Ford, and Tuscaloosa of the U.S. Gulf Coast: The Gulf Coast Association of Geological Societies Transactions, v. 60, p. 3-27.

Al Duhailan, M., Sonnenberg, S., and M. Longman, 2015, Analyzing "Beef" fractures: Genesis and relationship with organic-rich shale facies: Unconventional Resources Technology Conference (URTEC).

Algeo, T. J. and H. Rowe, 2012, Paleoceanographic applications of trace-metal concentration data: Chemical Geology, v. 324-325, p. 6-18.

Algeo, T. J. and J.B. Maynard, J. B., 2004, Trace-element behavior and redox facies in core shales of Upper Pennsylvanian Kansas-type cyclothems: Chemical geology, v. 206(3-4), p. 289-318.

Allix, P., A. Burnham, M. Herron, and R. Kleinberg, 2010, Gas Shale, Oil Shale, and Oil-Bearing Shale: Similarities and Differences: AAPG Search and Discovery 90122.

Arthur, M. A., and B. B. Sageman, 2005, Sea-Level Control on Source-Rock Development: Perspectives from the Holocene Black Sea, the Mid-Cretaceous Western Interior Basin of North America, and the late Devonian Appalachian Basin: Society for Sedimentary Geology, v. 82, p. 35-59.

Bohacs, K. M., G. J. Grabowski, A. R. Carrol, P. J. Mankiewicz, K. J. Miskell-Gerhardt, J. R. Schwalbach, and M. B. Wegner, 2005, Production, Destruction, and Dilution- the many Paths to Source-Rock Development: Society for Sedimentary Geology. v. 82, p. 61-101.

Brumsack, H.J., 1989, Geochemistry of recent TOC-rich sediments from the Gulf of California and the Black Sea: Geologische Rundschau, v. 78, no. 3, p. 851-882.

Brumsack, H. J., 2006, Trace metal content of recent organic carbon-rich sediments: Implications for Cretaceous black shale formation: Palaeogeophraphy, Palaeclimatology, Palaeoecology, v. 232, p. 344-361.

Cobbold, P.R., and N. Rodrigues, 2007, Seepage forces, important factors in the formation of horizontal hydraulicfractures and bedding-parallel fibrous veins (‘beef ’ and ‘cone-in-cone’): Geofluids, 7, p. 313–332.

Cusak, C. J., J. Beeson, D. Stoneburner, and G. Robertson, 2010, The discovery, reservoir attributes, and significance of the Hawkville Field and Eagle Ford Shale trend, Texas: Gulf Coast Association of Geologic Societies Transactions, v. 60, p. 165-179.

Deluca, M.J., 2016, Ash Bed Analysis of the Cretaceous Eagle Ford Shale Using ID-TIMS U-PB Methods: Implications for Biostratigraphic Refinement and Correlations within the Western Interior Seaway: Unpublished Master’s Thesis, Texas A&M University, Department of Geology 68 pp.

Demaison, G. J. and G.T. Moore, 1980, Anoxic Environments and Oil Source Bed Genesis: The American Association of Petroleum Geologists Bulletin, v. 64, i. 8, p. 1179-1209.

Denne, R. A. and J.A. Breyer, J., 2016, Regional Depositional Episodes of Cenomanian-Turonian Eagle Ford and Woodbine Groups of Texas. In R. A. Denne and J. A. Breyer, The Eagle Ford Shale: A renaissance in U.S. oil production: AAPG Memoir 110, p. 87-133.

Donovan, A. D., T.S. Staerker, A. Pramudito, W. Li, and M.J. Corbett, 2012, The Eagle Ford Outcrops of West Texas: A Laboratory for Understanding Heterogeneities within Unconventional Mudstone Reservoirs: Gulf Coast Association of Geological Societies Transactions, v. 1, p. 162-185.

Donovan, A. D., R.D. Gardner, A. Pramudito, T.S. Staerker, M. Wehner, M.J. Corbett, K.S. and Boling, 2015, Chronostratigraphic relationships of the Woodbine and Eagle Ford Groups across Texas: Gulf Coast Association of Geological Societies Transactions, v. 4, p. 67-87.

Donovan, A. D., T.S. Staerker, R. Gardner, M.C. Pope, M. C., A. Pramudito, and M. Wehner, 2016, Findings from the Eagle Ford Outcrops of West Texas and Implications to the Subsurface of South Texas: In R. A. Denne and J. A. Breyer, The Eagle Ford Shale: A renaissance in U.S. oil production: AAPG Memoir 110, p. 301-336.

Donovan, A.D., 2017, Personal communication: Unconventional Reservoirs Professor of Practice, Texas A&M University, Department of Geology.

Galloway, W.E., 2008, Depositional Evolution of the Gulf of Mexico sedimentary basin: Sedimentary basins of the world, v. 5, p. 505-549.

Harris, N. B., 2005, The deposition of organic-carbon-rich-sediments: models, mechanisms, and consequences: Society for Sedimentary Geology, p. 35-59.

Hentz, T. F. and S.C. Ruppel, 2010, Regional lithostratigraphy of the Eagle Ford Shale: Maverick Basin to East Texas Basin: Gulf Coast Association of Geological Societies Transactions, v. 60, p. 325-337.

Hentz, T. F. and S.C. Ruppel, S. C., 2011, Regional stratigraphic and rock characteristics of Eagle Ford Shale in its play area: Maverick Basin to east Texas Basin: AAPG Annual Convention and Exhibition, v. 10, p. 13.

Hentz, T. F., W. A. Ambrose, and D. C. Smith, 2014, Eaglebine play of southwestern East Texas basin: Stratigraphic and depositional framework of the Upper Cretaceous (Cenomanian-Turonian) Woodbine and Eagle Ford Groups: AAPG Bulletin, v. 98, no. 12, p. 2551-2580.

Hollander, D. B., M. Vandernbroucke, P. Bertrand, and J.A. McKenzie, 1991, Geochemical alteration of organic matter in eutrophic Lake Greifen: implications for the determination of organic facies and the origin of lacustrine source rocks: American Association of Petroleum Geologists, Studies in Geology, v. 30, p. 181-193.

Hudson, A. M., 2014, Stratigraphy and Depositional Controls on Source Rock Formation within the Upper Cretaceous (Lower Cenomanian) Maness Shale, Central Texas: Master's Thesis, Texas A&M University, Department of Geology.

IHS Energy Group, 2018, U.S. well and production data: Englewood, Co, IHS Energy Group.

Katz, B. J., 2012, Controlling Factors on Source Rock Development- A Review of Productivity, Preservation, and Sedimentation Rate: Society for Sedimentary Geology Special Publications, v. 82, p. 7-16.

Kearns, T. J., 2011, Chemostratigraphy of the Eagle Ford Formation: Master's Thesis, The University of Texas Arlington, Department of Geology.

Kruse, K. R., 2014, Paleoenvironmental controls on diagenesis of organic-rich shales in the Eagle Ford Group: Master's Thesis, Texas A&M University, Department of Geology.

Lee, J. S., Smallwood, L., and E. Morgan, 2014, New application of rebound hardness numbers to generate logging of unconfined compressive strength in laminated shale formations: ARMA, v. 14-6972, p. 7.

Lewan, M. D. and J.B. Maynard, J. B., 1982, Factors controlling enrichment of vanadium and nickel in the bitumen of organic sedimentary rocks: Geochimica et Cosmochimica Acta, v. 46, no. 12, p. 2547-2560.

Mancini, E. A., P. Li, D. A. Goddard, V. Ramirez, and S. C. Talukdar, 2008, Mesozoic (Upper Jurassic-Lower Cretaceous) deep gas reservoir play, central and eastern gulf coastal plain: AAPG Bulletin, v. 92, p. 283-308.

McCallum, H. D., 1933, Darst Creek oil field, Guadalupe County, Texas: AAPG Bulletin, v. 17, p. 16-37.

Moran, L. M., 2013, High resolution geochemistry of the Cretaceous Eagle Ford Formation, Bee County, Texas: Master's Thesis, The University of Texas at Arlington, Department of Geology.

Pearce, T. J., and I. Jarvis, 1992, Applications of geochemical data to modelling sediment dispersal patterns in distal turbidites: Late Quaternary of the Madeira Abyssal Plain: Journal of Sedimentary Petrology, v. 62, p. 1112-1129.

Ratcliffe, K. T., Morton, A. C., Ritcey, D. H., and C. A. Evenchick, 2007, Whole-rock geochemistry and heavy mineral analysis as petroleum exploration tools in the Bowser and Sustut basins, British Columbia, Canada: Bulletin of Canadian Petroleum Geology, v. 55, p. 320-336.

Ratcliffe, G. H., and K. Schmidt, 2011, Application of inorganic whole-rock geochemistry to shale resource plays: an example from the Eagle Ford Shale, Texas: Houston Geological Society Bulletin, v. 53, no. 8, p. 31-37.

Romesburg, H. C., 1989, Cluster analysis for researchers: Lulu Press, p. 333.

Roush, R. S., 2015, Regional stratigraphic and core-based characterization of the Cline Shale, Midland Basin, Texas: Doctoral Dissertation, The University of Texas at Austin, Department of Geological Sciences.

Rowe, H. D., N. Hughes, and K. Robinson, 2012, The quantification and application of handheld energy-dispersive x-ray fluorescence (ED-XRF) in mudrock chemostratigraphy and geochemistry: Chemical Geology, v. 324-325, p. 122-131.

Sageman, B. B., and T.W., Lyons, 2004, Geochemistry of fine-grained sediments and sedimentary rocks: Sediments, Diagenesis, and Sedimentary Rocks, v. 7, p115-158.

Vallabhaneni, S., T.D. Olszewski, M.C. Pope, and Z. Heidari, Z, 2016, Facies and Stratigraphic Interpretation of the Eaglebine Play in Central Texas: Gulf Coast Association of Geological Societies Transactions, v. 5, p. 25-46.

Taylor, S. R., and S. M. P, 1985, The Continental Crust: its Composition and Evolution. Oxford: Blackwell Scientific Publications, p. 312.

Temple, M., P. Filzmoser, C. Reimann, 2008, Cluster analysis applied to regional geochemical data – problems and possibilities: Applied Geochemistry, v. 23, p. 2198–2213.

Tinnin, B. M., and T. R. Darmaoen, 2016, Chemostratigraphic Variability of the Eagle Ford Shale, South Texas: Insights into Paleoredox and Sedimentary Facies Changes. In J. A. Breyer, The Eagle Ford Shale: A renaissance in U.S. oil production: AAPG Memoir 110, p. 259-285.

Tribovillard, N., T.J. Algeo, T. Lyons, and A. Riboulleau, 2006, Trace Metals as Paleoredox and Paleoproductivity Proxies: An Update: Chemical Geology, v. 232, p. 12-32.

Tyson, R. V., 2005, The "Productivity versus Preservation" Controversy: cause, flaws, and resolution: Society for Sedimentary Geology Special Publications, v. 82, p. 17-33.

U.S. Energy Information Administration, 2016, Annual Energy Outlook 2016 with projections to 2040, https://www.eia.gov/outlooks/aeo/pdf/0383(2016).pdf, 11/1/2017.

Wedepohl, K.H., 1970, Environmental influences on the chemical composition of shales and clays: Physics and Chemistry of the Earth, v. 8, p. 305-333.

Wehner, M., R.D. Gardner, M.C. Pope, and A.D. Donovan, 2017, The Eagle Ford Group Returns to Big Bend National Park, Brewster County, Texas: Gulf Coast Association of Geological Societies Transactions, v. 6, p. 161-176.

Zeng, Z., and M.M. Tice, 2014, Promotion and nucleation of carbonate precipitation during microbial iron reduction: Geobiology, v. 12, p. 362-371.

APPENDIX A

GEOLOGIC PROFILES

CORE A

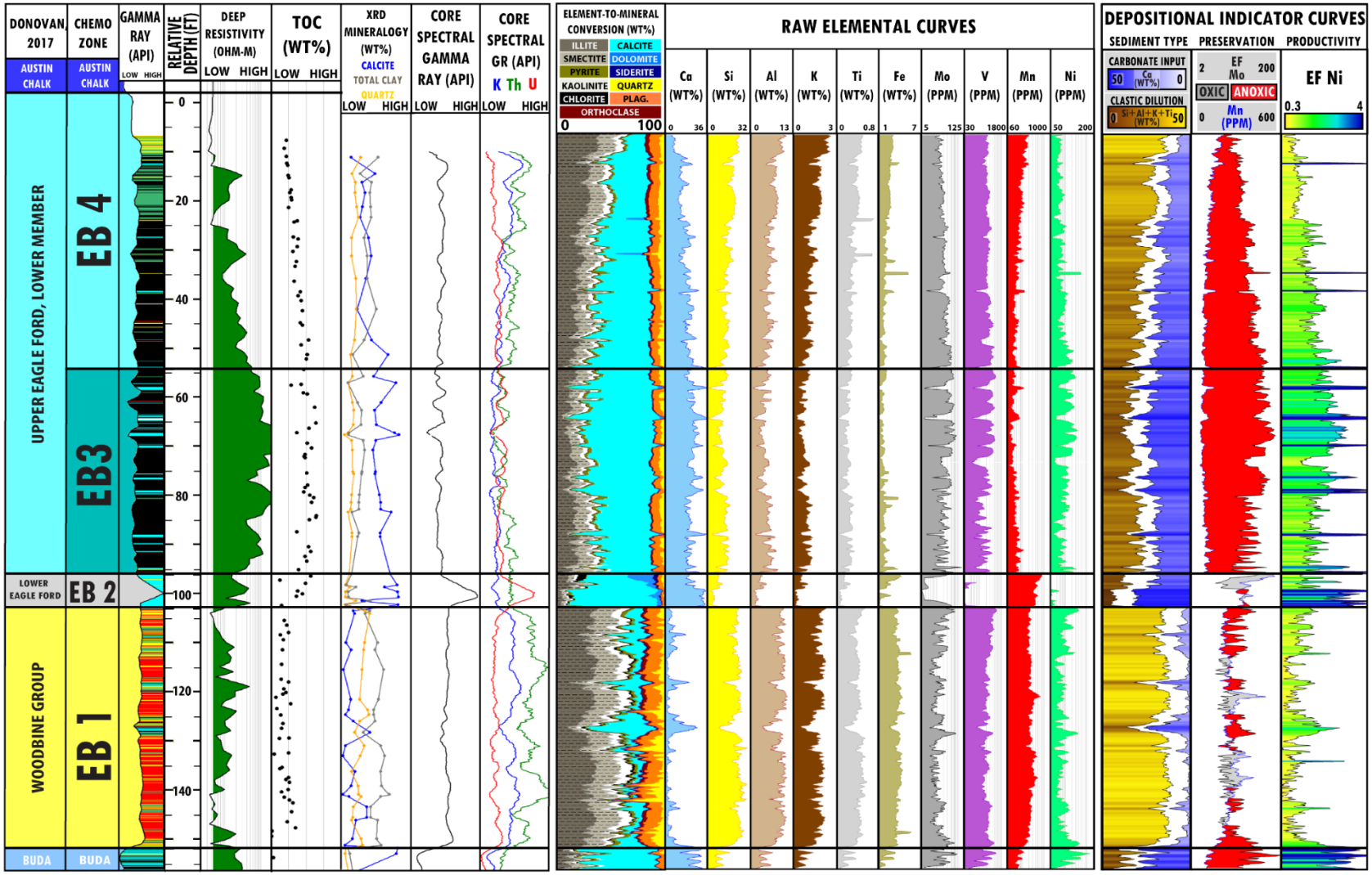

Figure A1. Geochemical profiles for Core A correlated to TOC, XRD mineralogy, gamma-ray, and deep-resistivity logs. Depositional indicator curves are key curves that indicate variations in OM dilution, preservation, and productivity. Chemofacies color legend is shown in Figure 5. EF = enrichment factor.

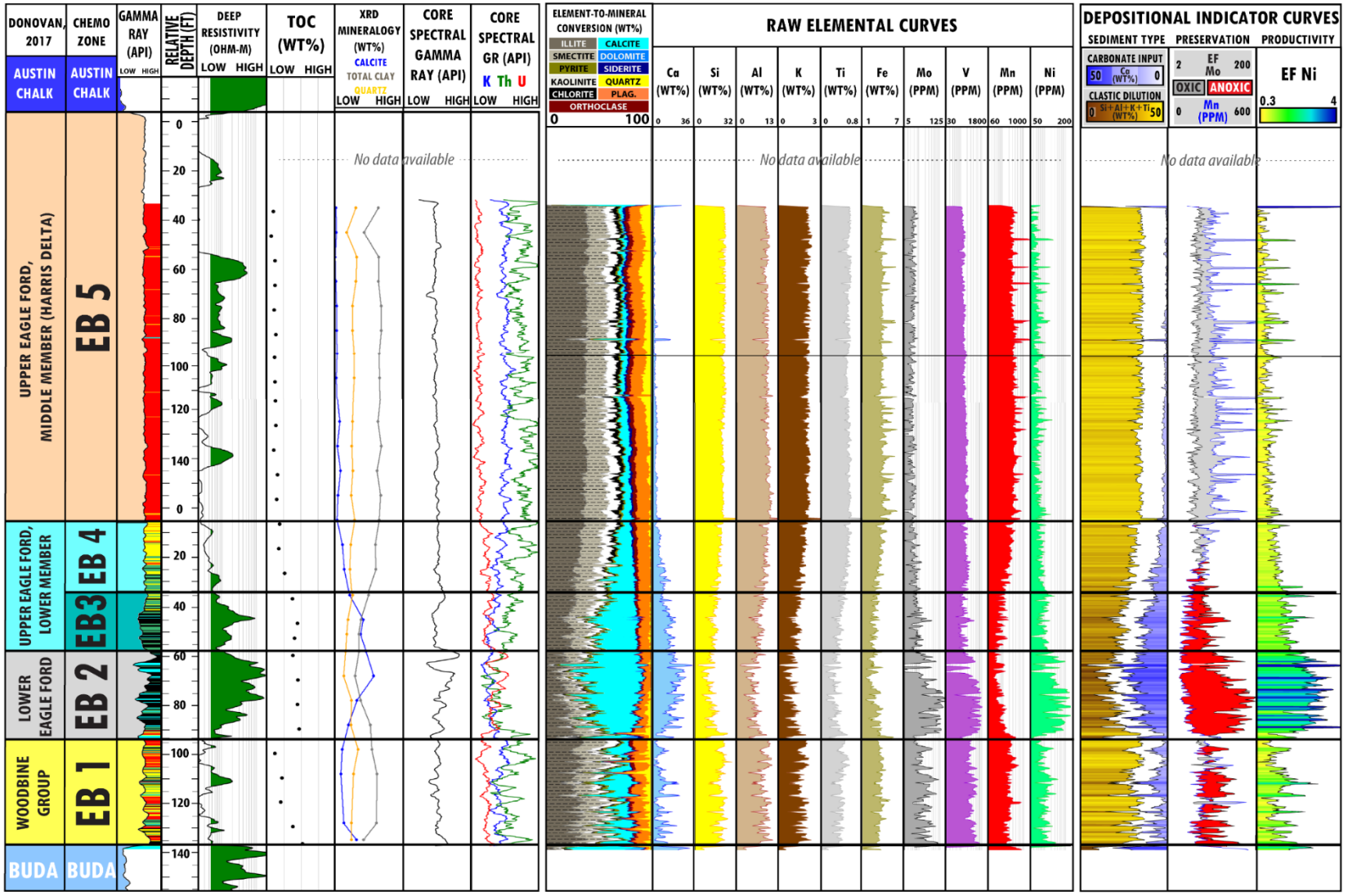

Figure A2. Geochemical profiles for Core B correlated to TOC, XRD mineralogy, gamma-ray, and deep-resistivity logs. Depositional indicator curves are key curves that indicate variations in OM dilution, preservation, and productivity. Chemofacies color legend is shown in Figure 5. EF = enrichment factor.

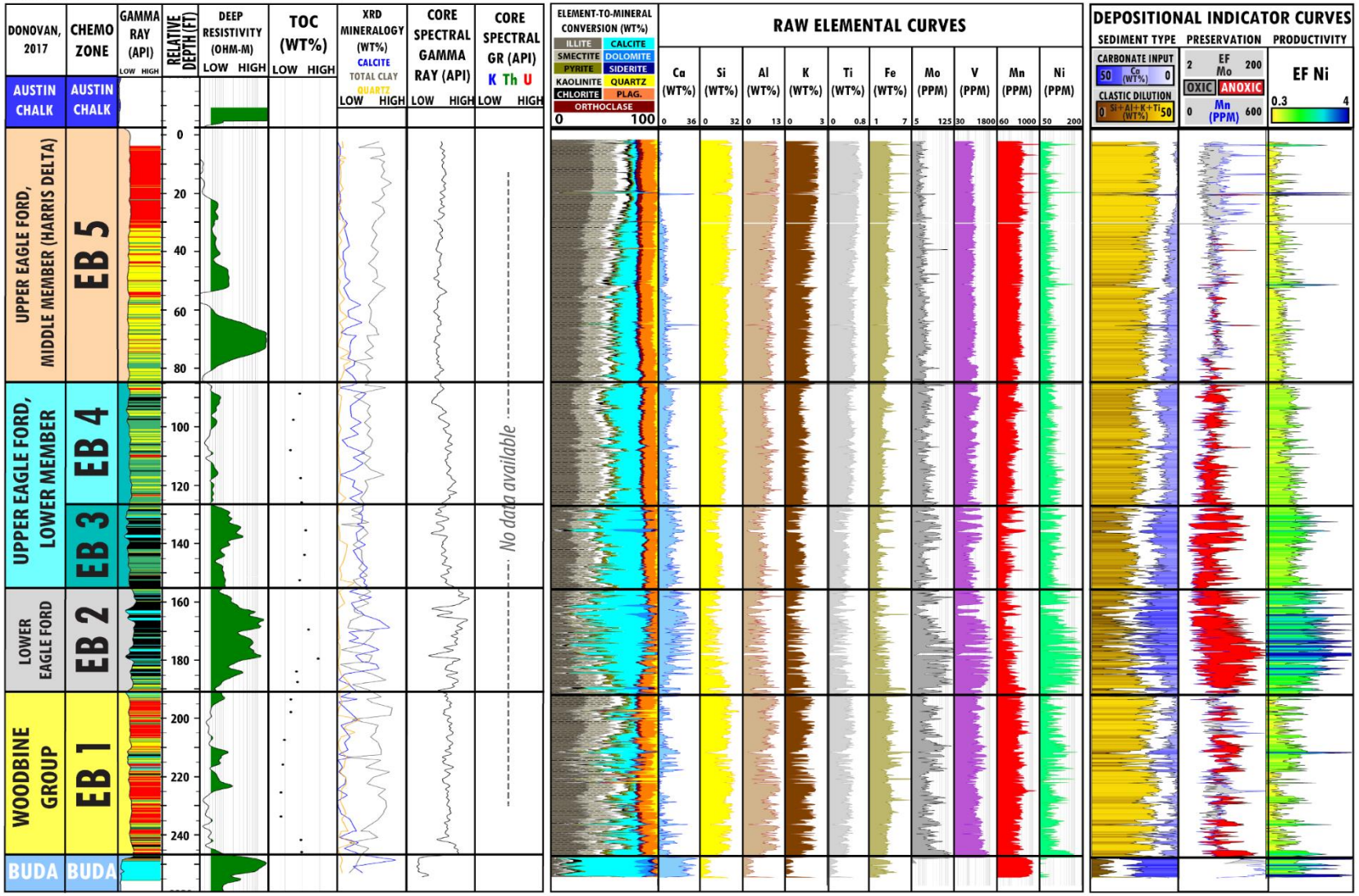

Figure A3. Geochemical profiles for Core C correlated to TOC, XRD mineralogy, gamma-ray, and deep-resistivity logs. Depositional indicator curves are key curves that indicate variations in OM dilution, preservation, and productivity. Chemofacies color legend is shown in Figure 5. EF = enrichment factor.

CORE D

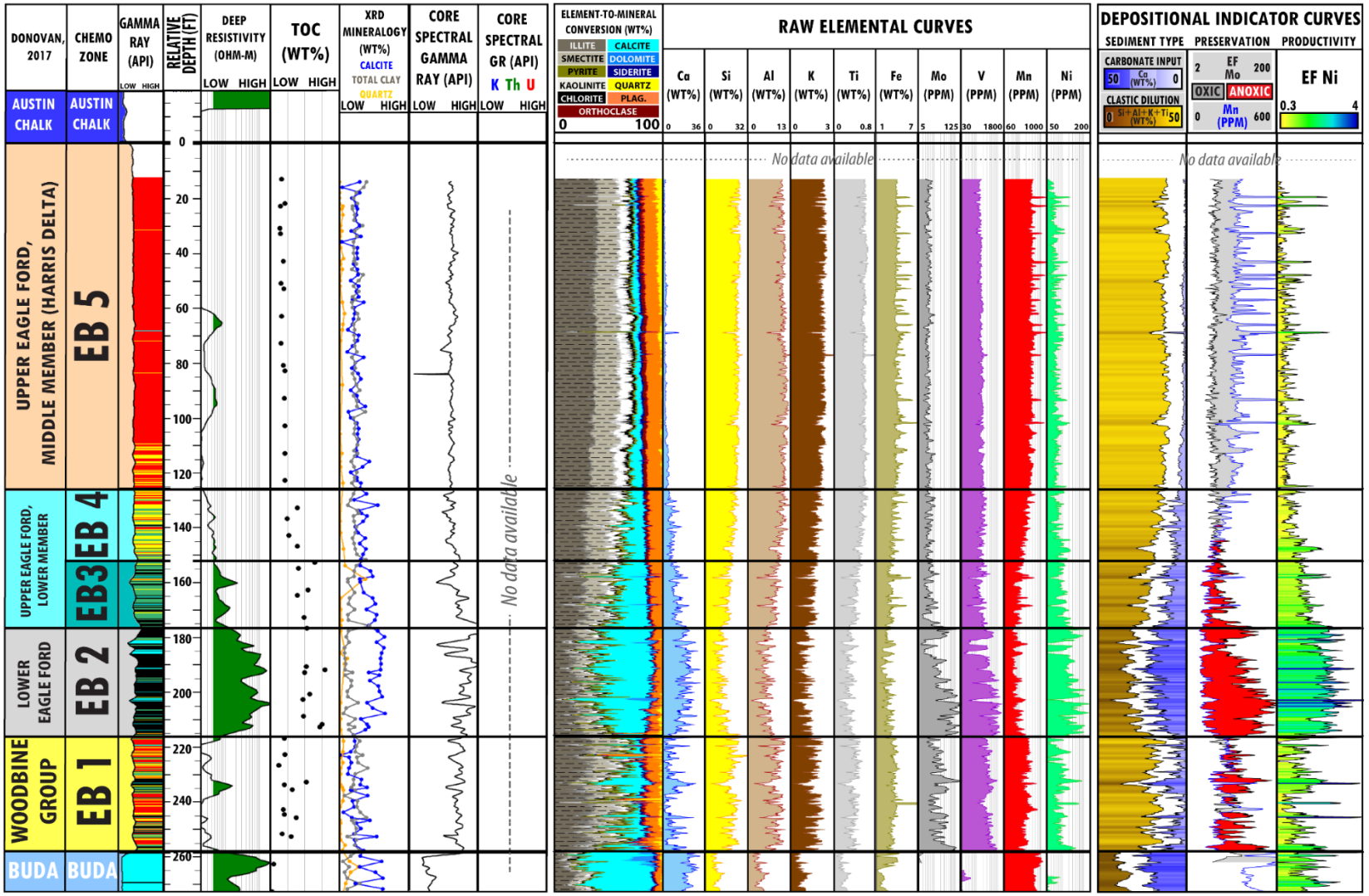

Figure A4. Geochemical profiles for Core D correlated to TOC, XRD mineralogy, gamma-ray, and deep-resistivity logs. Depositional indicator curves are key curves that indicate variations in OM dilution, preservation, and productivity. Chemofacies color legend is shown in Figure 5. EF = enrichment factor.

CORE E

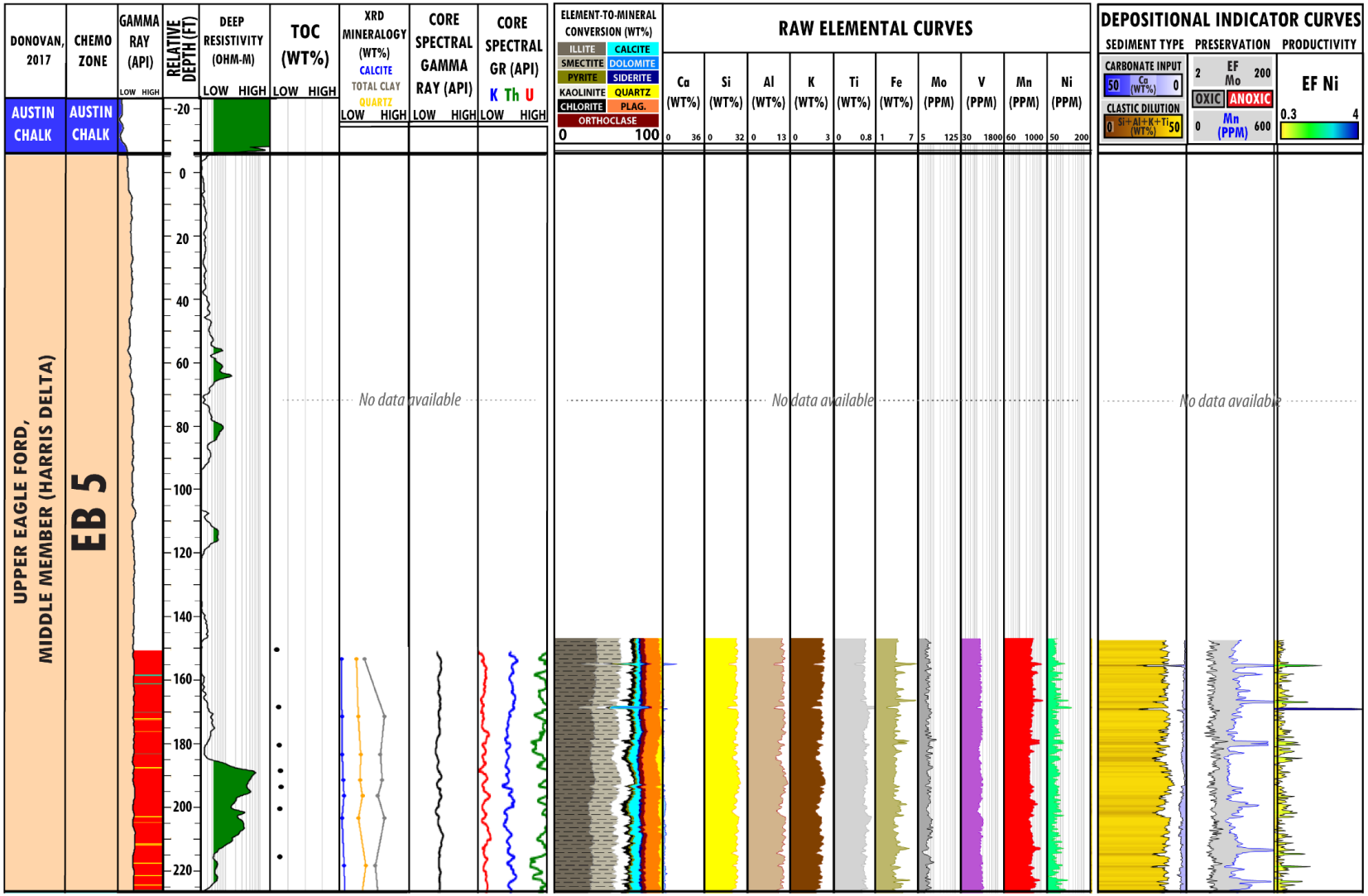

Figure A5. Geochemical profiles for Core E correlated to TOC, XRD mineralogy, gamma-ray, and deep-resistivity logs. Depositional indicator curves are key curves that indicate variations in OM dilution, preservation, and productivity. Chemofacies color legend is shown in Figure 5. EF = enrichment factor.

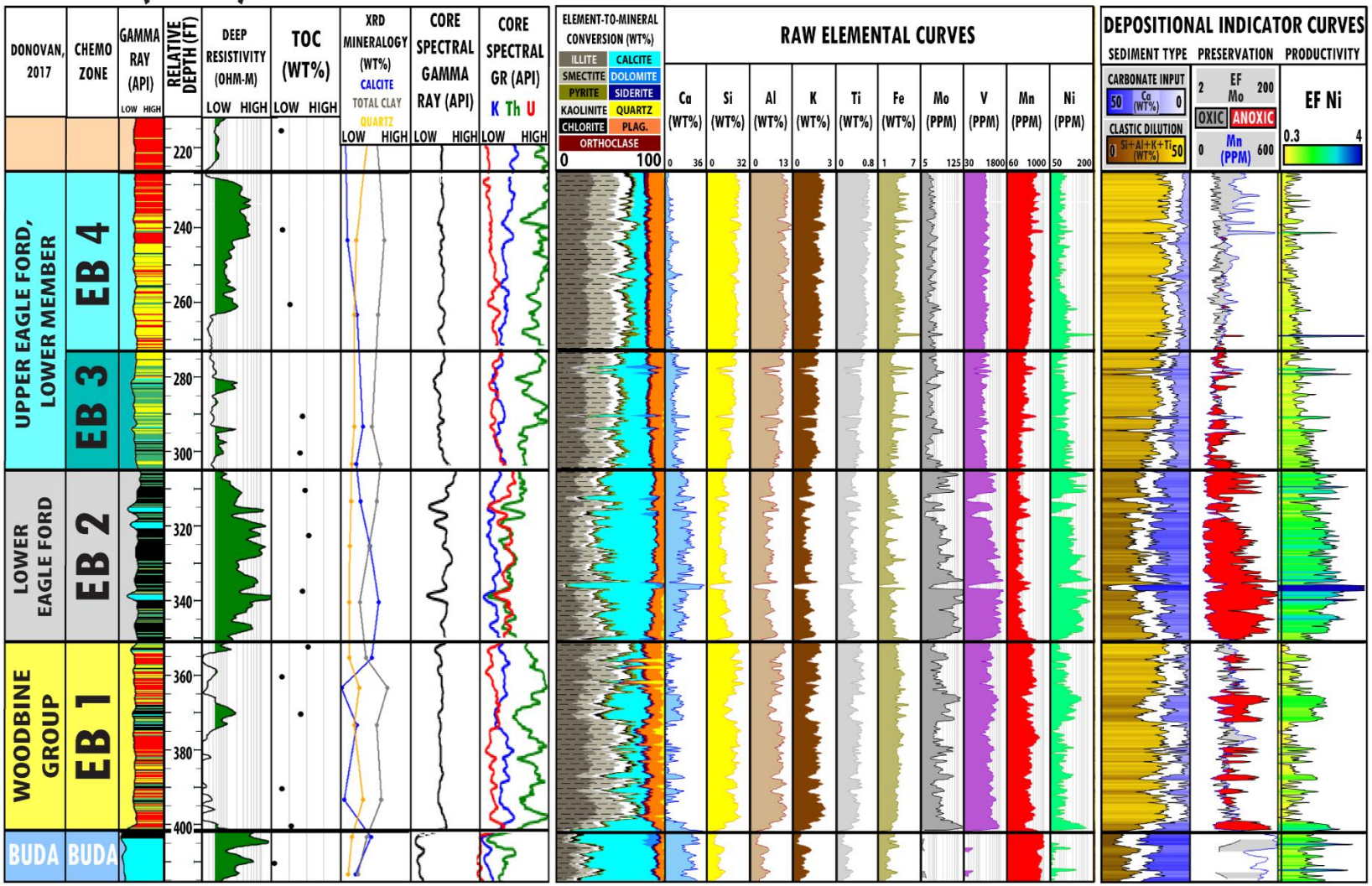

Figure A6. Geochemical profiles for Core E correlated to TOC, XRD mineralogy, gamma-ray, and deep-resistivity logs. Depositional indicator curves are key curves that indicate variations in OM dilution, preservation, and productivity. Chemofacies color legend is shown in Figure 5. EF = enrichment factor.

CORE F

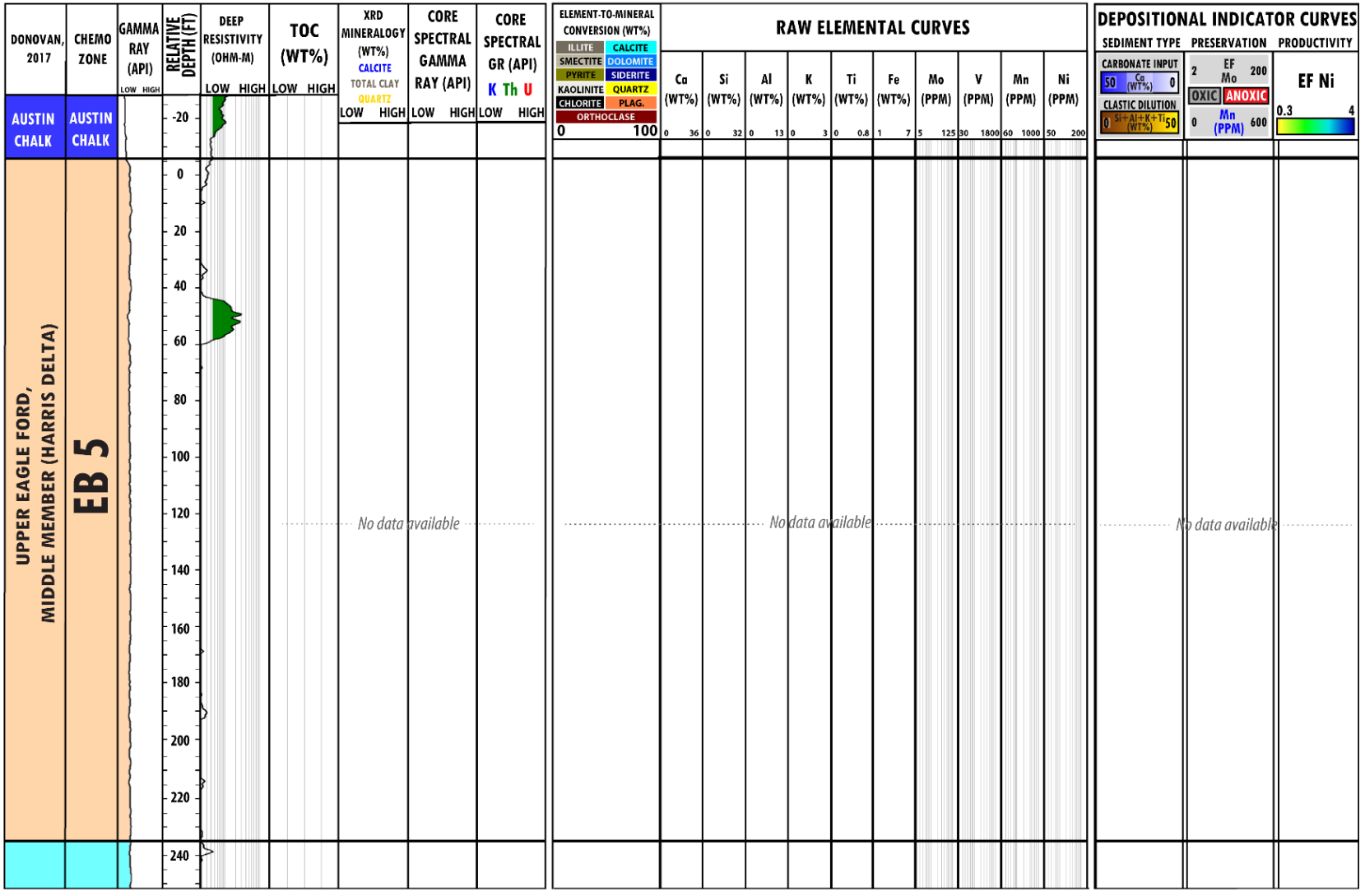

Figure A7. Geochemical profiles for Core F correlated to TOC, XRD mineralogy, gamma-ray, and deep-resistivity logs. Depositional indicator curves are key curves that indicate variations in OM dilution, preservation, and productivity. Chemofacies color legend is shown in Figure 5. EF = enrichment factor.

CORE F (cont.)

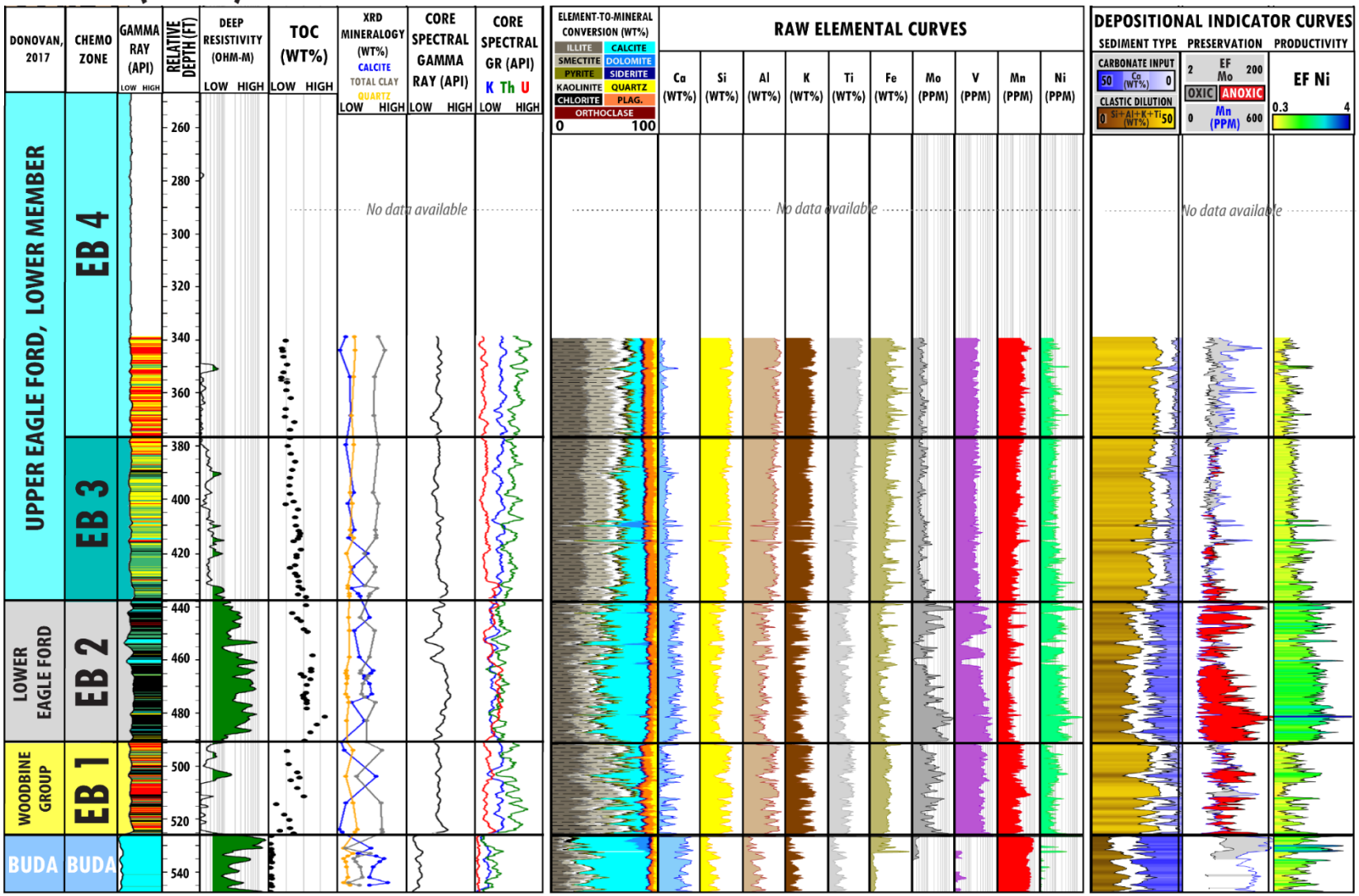

Figure A8. Geochemical profiles for Core F correlated to TOC, XRD mineralogy, gamma-ray, and deep-resistivity logs. Depositional indicator curves are key curves that indicate variations in OM dilution, preservation, and productivity. Chemofacies color legend is shown in Figure 5. EF = enrichment factor.

CORE G

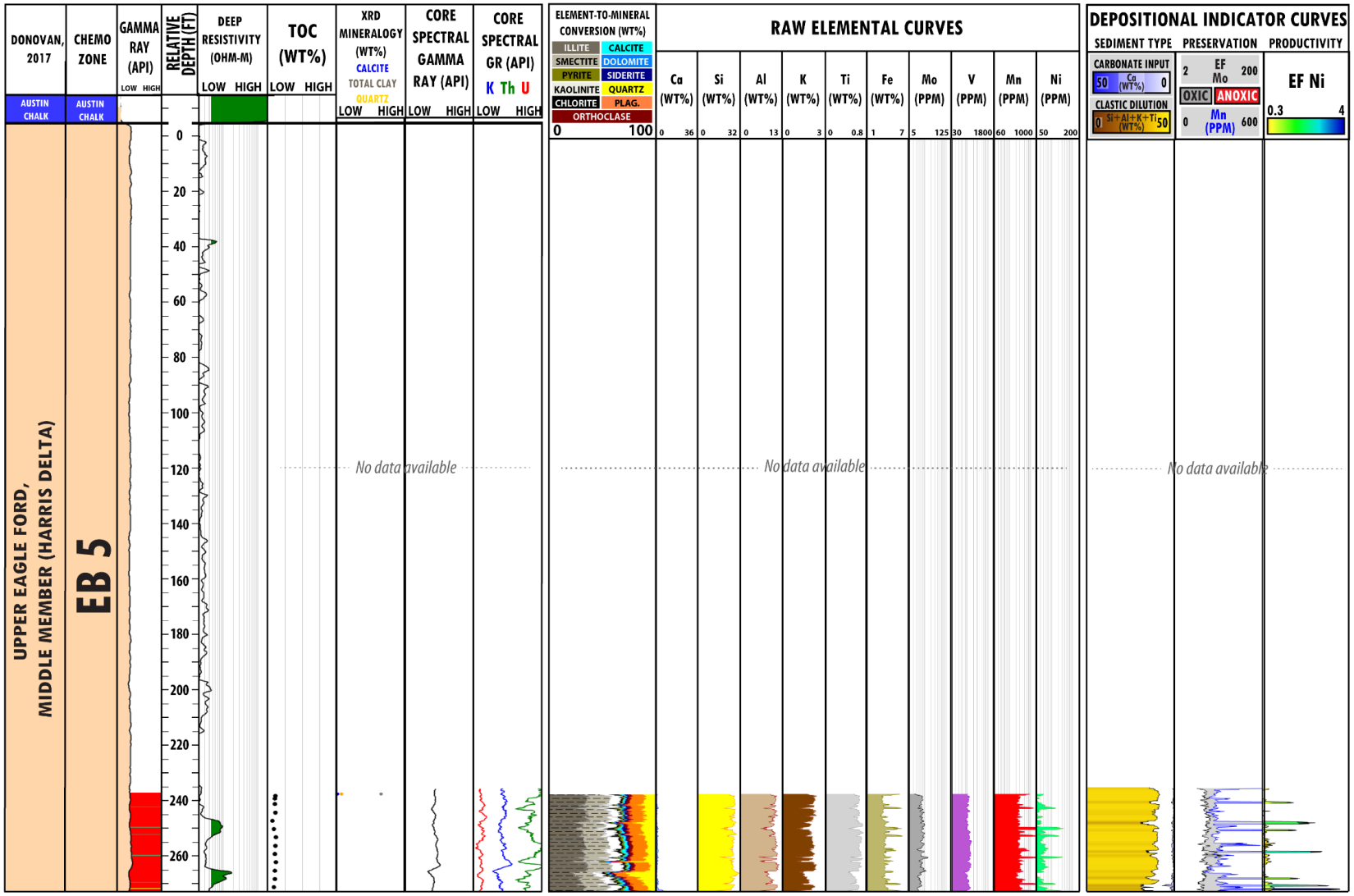

Figure A9. Geochemical profiles for Core G correlated to TOC, XRD mineralogy, gamma-ray, and deep-resistivity logs. Depositional indicator curves are key curves that indicate variations in OM dilution, preservation, and productivity. Chemofacies color legend is shown in Figure 5. EF = enrichment factor.

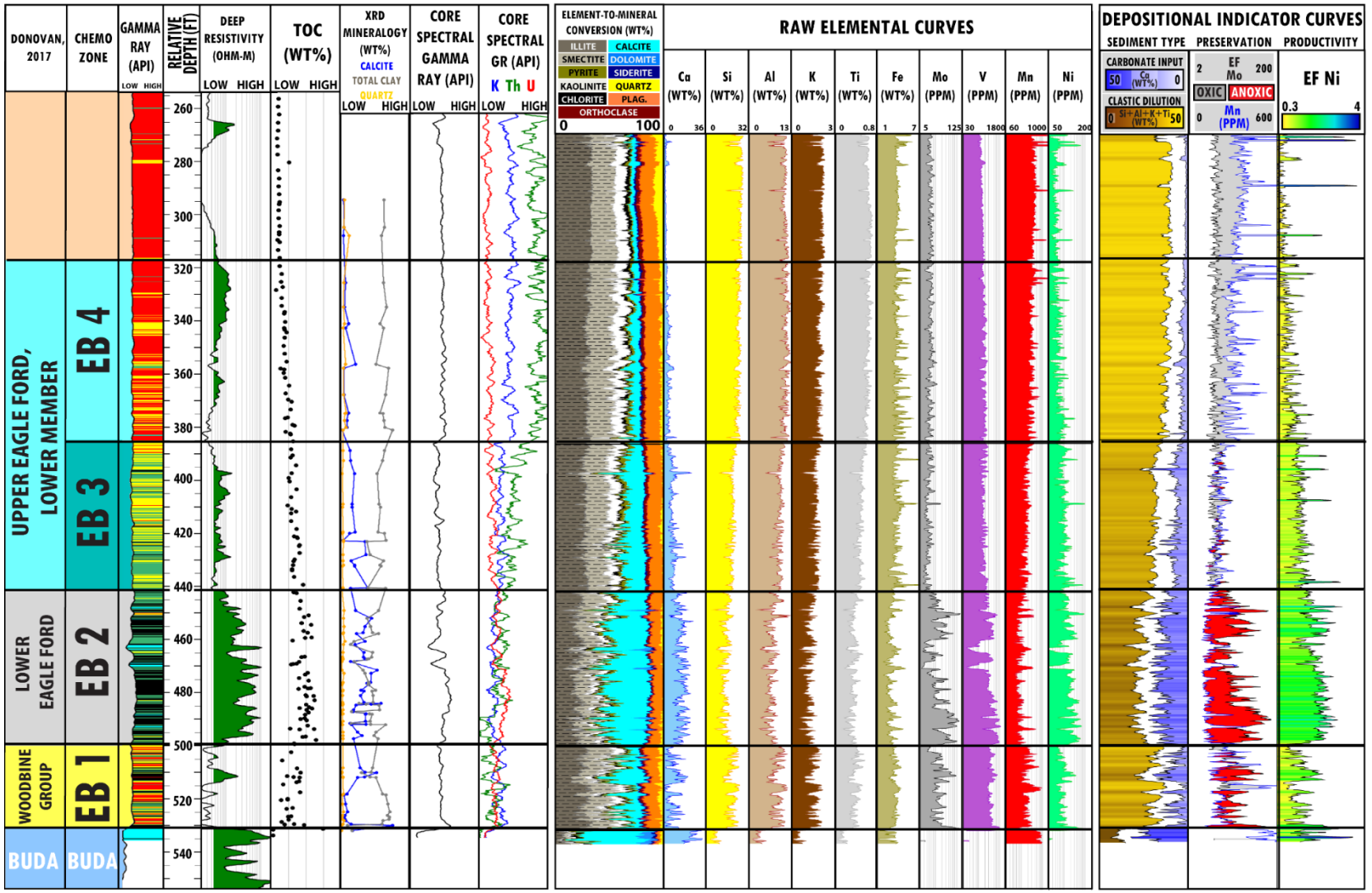

Figure A10. Geochemical profiles for Core G correlated to TOC, XRD mineralogy, gamma-ray, and deep-resistivity logs. Depositional indicator curves are key curves that indicate variations in OM dilution, preservation, and productivity. Chemofacies color legend is shown in Figure 5. EF = enrichment

CORE H

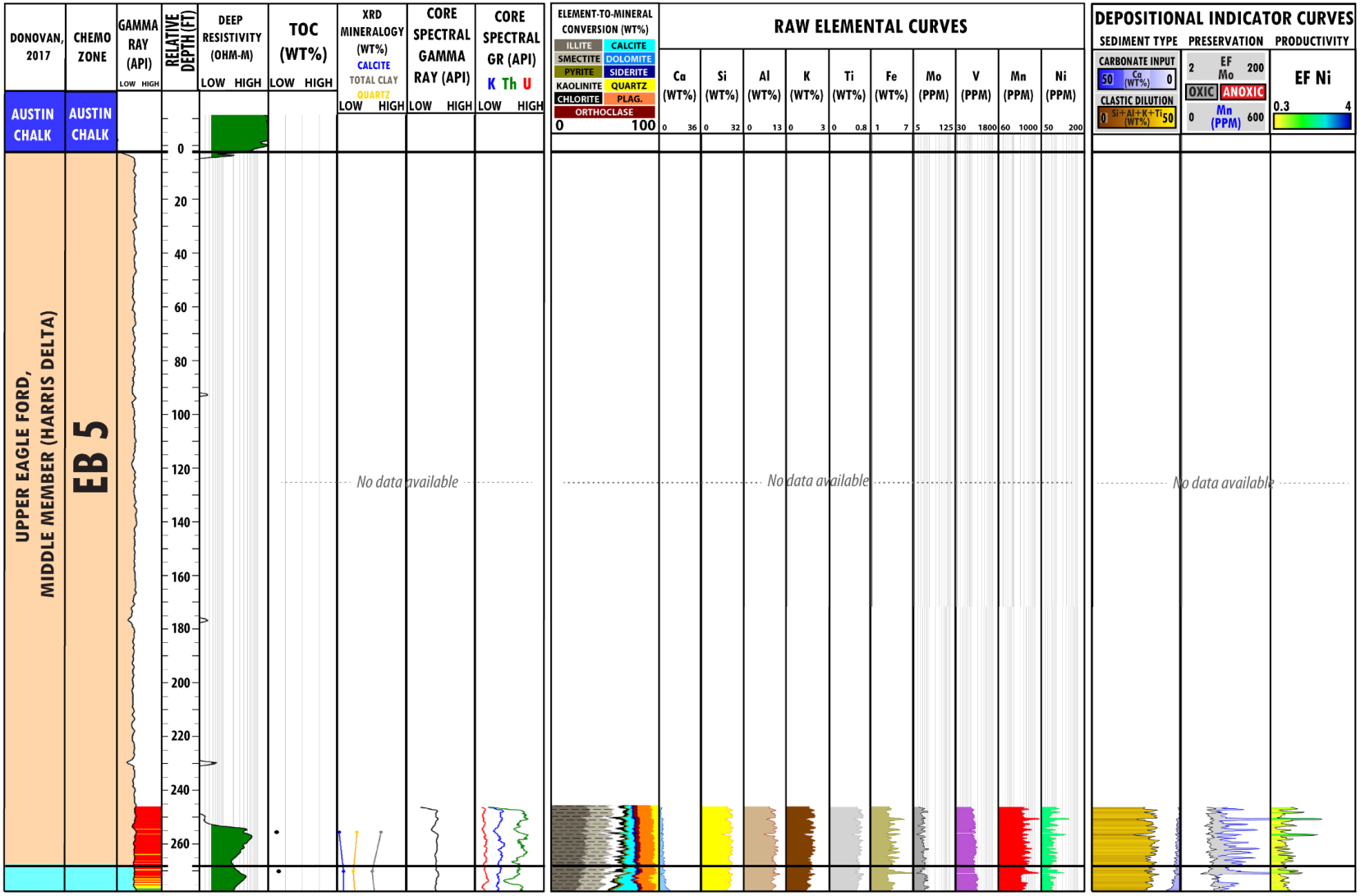

Figure A11. Geochemical profiles for Core G correlated to TOC, XRD mineralogy, gamma-ray, and deep-resistivity logs. Depositional indicator curves are key curves that indicate variations in OM dilution, preservation, and productivity. Chemofacies color legend is shown in Figure 5. EF = enrichment

CORE H (cont.)

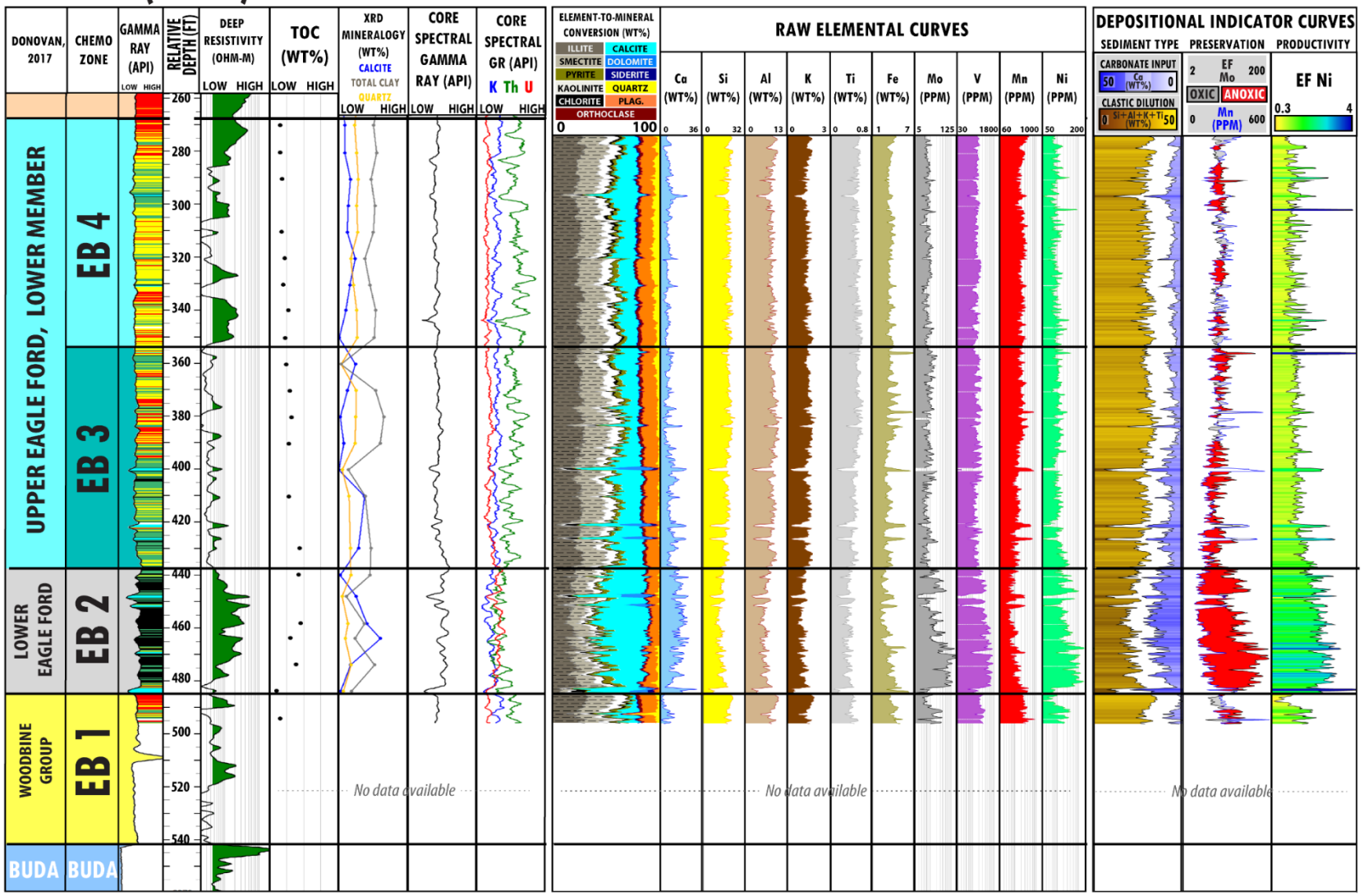

Figure A12. Geochemical profiles for Core H correlated to TOC, XRD mineralogy, gamma-ray, and deep-resistivity logs. Depositional indicator curves are key curves that indicate variations in OM dilution, preservation, and productivity. Chemofacies color legend is shown in Figure 5. EF = enrichment

CORE I

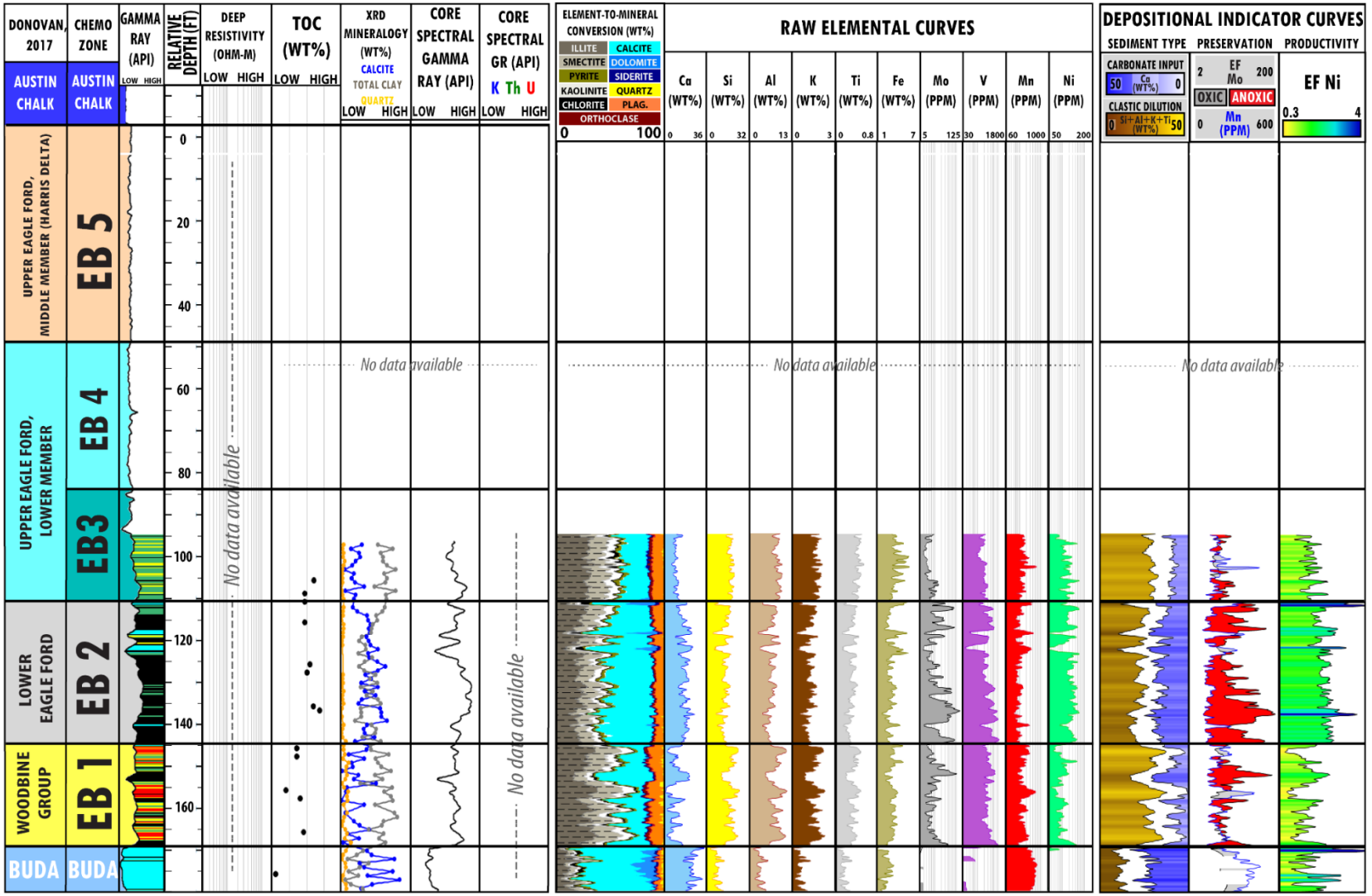

Figure A13. Geochemical profiles for Core I correlated to TOC, XRD mineralogy, gamma-ray, and deep-resistivity logs. Depositional indicator curves are key curves that indicate variations in OM dilution, preservation, and productivity. Chemofacies color legend is shown in Figure 5. EF = enrichment factor.

CORE J

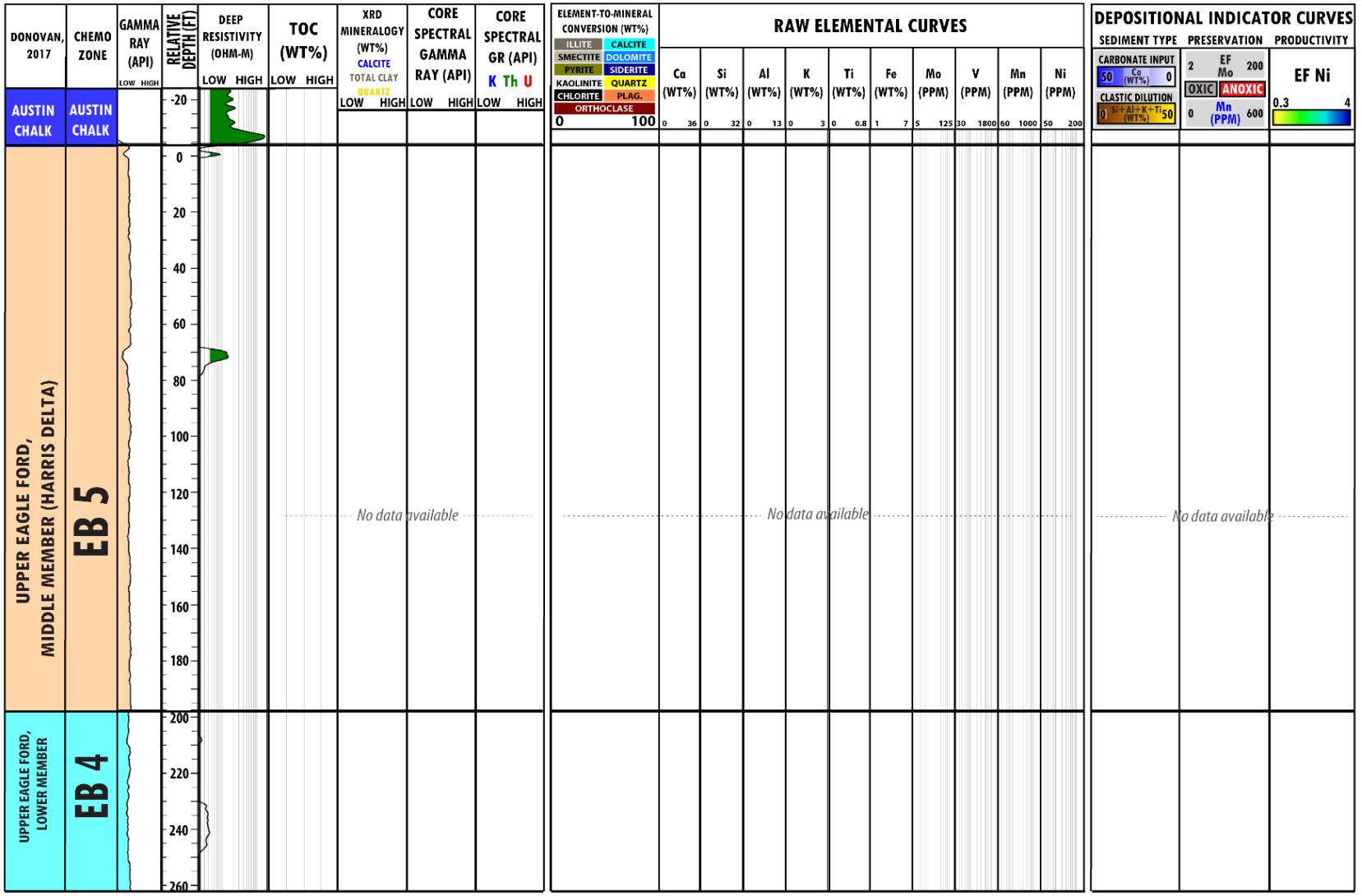

Figure A14. Geochemical profiles for Core J correlated to TOC, XRD mineralogy, gamma-ray, and deep-resistivity logs. Depositional indicator curves are key curves that indicate variations in OM dilution, preservation, and productivity. Chemofacies color legend is shown in Figure 5. EF = enrichment factor.

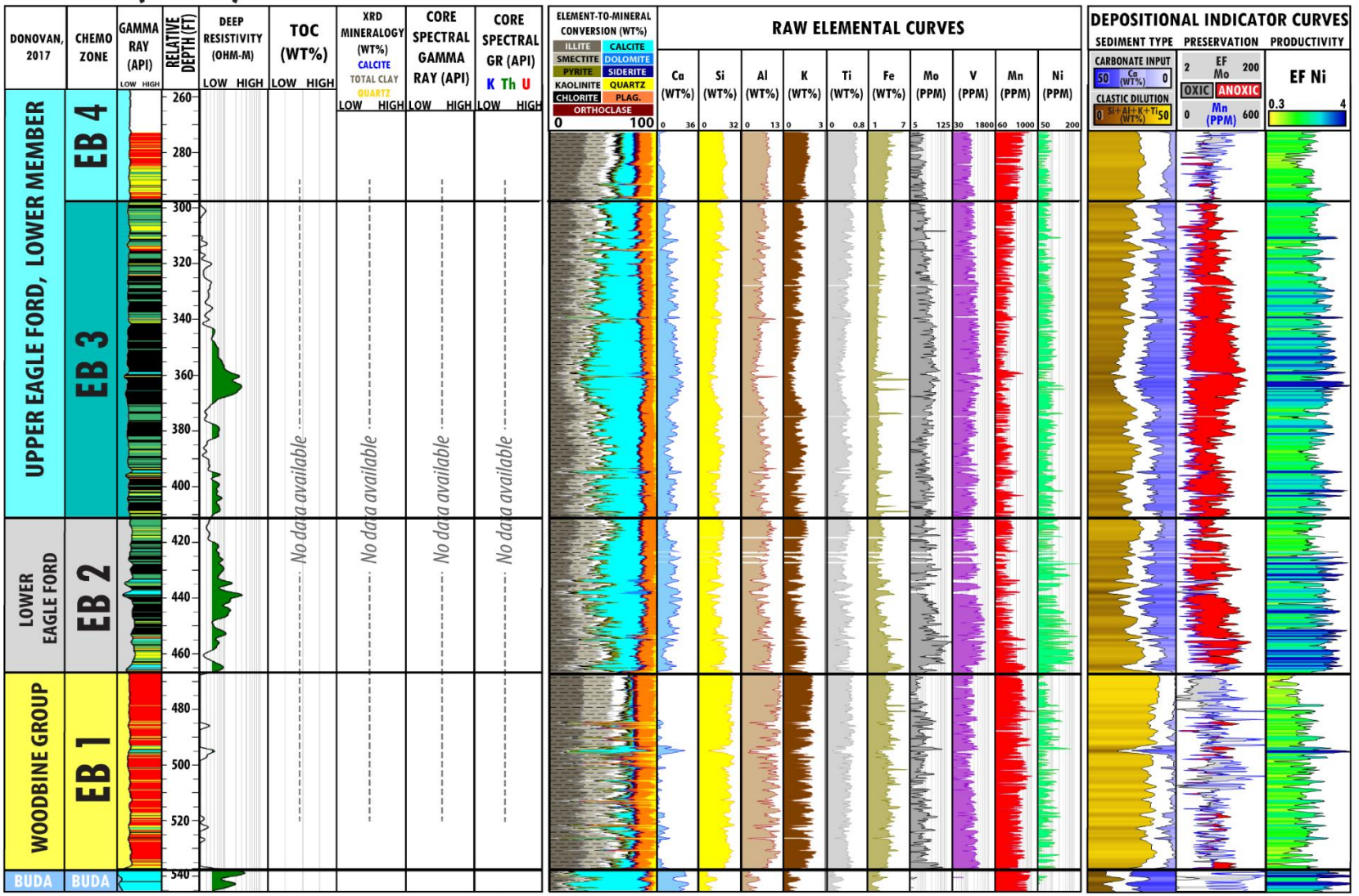

Figure A15. Geochemical profiles for Core J correlated to TOC, XRD mineralogy, gamma-ray, and deep-resistivity logs. Depositional indicator curves are key curves that indicate variations in OM dilution, preservation, and productivity. Chemofacies color legend is shown in Figure 5. EF = enrichment factor.